

# Constructions of ROS-responsive titanium-hydroxyapatite implant for mesenchymal stem cell recruitment in peri-implant space and bone formation in osteoporosis microenvironment

Maohua Chen<sup>a,1</sup>, Yuting Sun<sup>a,1</sup>, Yanhua Hou<sup>c</sup>, Zhong Luo<sup>b,\*</sup>, Menghuan Li<sup>b</sup>, Yujia Wei<sup>a</sup>,  
Maowen Chen<sup>a</sup>, Lu Tan<sup>a</sup>, Kaiyong Cai<sup>a,\*\*</sup>, Yan Hu<sup>a,\*\*\*</sup>

<sup>a</sup> Key Laboratory of Biorheological Science and Technology, Ministry of Education, College of Bioengineering, Chongqing University, Chongqing, 400044, China

<sup>b</sup> School of Life Science, Chongqing University, Chongqing, 400044, China

<sup>c</sup> Chongqing Engineering Research Center of Pharmaceutical Science, Chongqing Medical and Pharmaceutical College, Chongqing, 401331, China

## ARTICLE INFO

### Keywords:

Mesenchymal stem cell recruitment  
Osteogenic differentiation  
Hydroxyapatite  
Titanium  
Osteoporosis

## ABSTRACT

To solve the issue of unsatisfactory recruitment of mesenchymal stem cells (MSCs) around implant in osteoporotic fractures, we fabricated a ROS-responsive system on titanium surface through hydroxyapatite coating and biomolecule grafting. The porous hydroxyapatite and phosphorylated osteogenic growth peptides (*p*-OGP) were introduced onto titanium surface to synergistically improve osteogenic differentiation of MSCs. After the *p*-OGP-promoted expression of osteogenic related proteins, the calcium and phosphate ions were released through the degradation of hydroxyapatite and integrated into bone tissues to boost the mineralization of bone matrix. The ROS-triggered release of DNA aptamer (Apt) 19S in the osteoporotic microenvironment guides MSC migration to implant site due to its high affinity with alkaline phosphatase on the membrane of MSCs. Once MSCs reached the implant interface, their osteogenic differentiation potential was enhanced by *p*-OGP and hydroxyapatite to promote bone regeneration. The study here provided a simple and novel strategy to prepare functional titanium implants for osteoporotic bone fracture repair.

## 1. Introduction

Titanium and its alloys are extensively used in the medical field accounting on their good biomechanical properties and biocompatibility [1,2]. However, the poor osseointegration of titanium implants may severely compromise the efficacy of fracture healing [3,4], especially for patients with osteoporosis. Early loosening of implants is common severe complication in osteoporosis patients, which often necessitates the secondary surgery [5,6]. Therefore, it's crucially important to improve the early bone healing of the implants. Many strategies have been developed to endow titanium substrates with bioactivity, which mainly include various mechanical or physicochemical treatment or introduction of biomolecules cues on the titanium surface. These strategies have great effects on the behavior of osteoblast cells, especially mesenchymal

stem cells (MSCs).

During osteoporotic fracture repair, osteoblastic differentiation of bone marrow MSCs plays an important role in bone repair and bone remodeling [7]. When bone injury occurs, MSCs migrate from bone marrow or other adjacent tissues to the site of bone injury and secrete paracrine nutrients [8–10]. Meanwhile, MSCs also participate in the healing process of inflammatory, repair, and remodeling together with progenitor cells, stromal cells, pro-inflammatory and anti-inflammatory macrophages [11,12]. After their directed differentiation into osteoblasts, MSCs secrete major components of extracellular bone matrix such as osteocalcin, osteopontin, type I collagen to promote the in-situ deposition of calcium ions, leading to the formation of hard tissues [13,14]. Therefore, the number of MSCs in the site of bone injury and their ability to differentiate into osteoblasts are directly related to the

Peer review under responsibility of KeAi Communications Co., Ltd.

\* Corresponding author.

\*\* Corresponding author.

\*\*\* Corresponding author.

E-mail addresses: [luozhong918@cqu.edu.cn](mailto:luozhong918@cqu.edu.cn) (Z. Luo), [kaiyong\\_cai@cqu.edu.cn](mailto:kaiyong_cai@cqu.edu.cn) (K. Cai), [huyan303@cqu.edu.cn](mailto:huyan303@cqu.edu.cn) (Y. Hu).

<sup>1</sup> Authors contributed equally to the work.

<https://doi.org/10.1016/j.bioactmat.2022.02.006>

Received 4 June 2021; Received in revised form 17 January 2022; Accepted 8 February 2022

Available online 19 February 2022

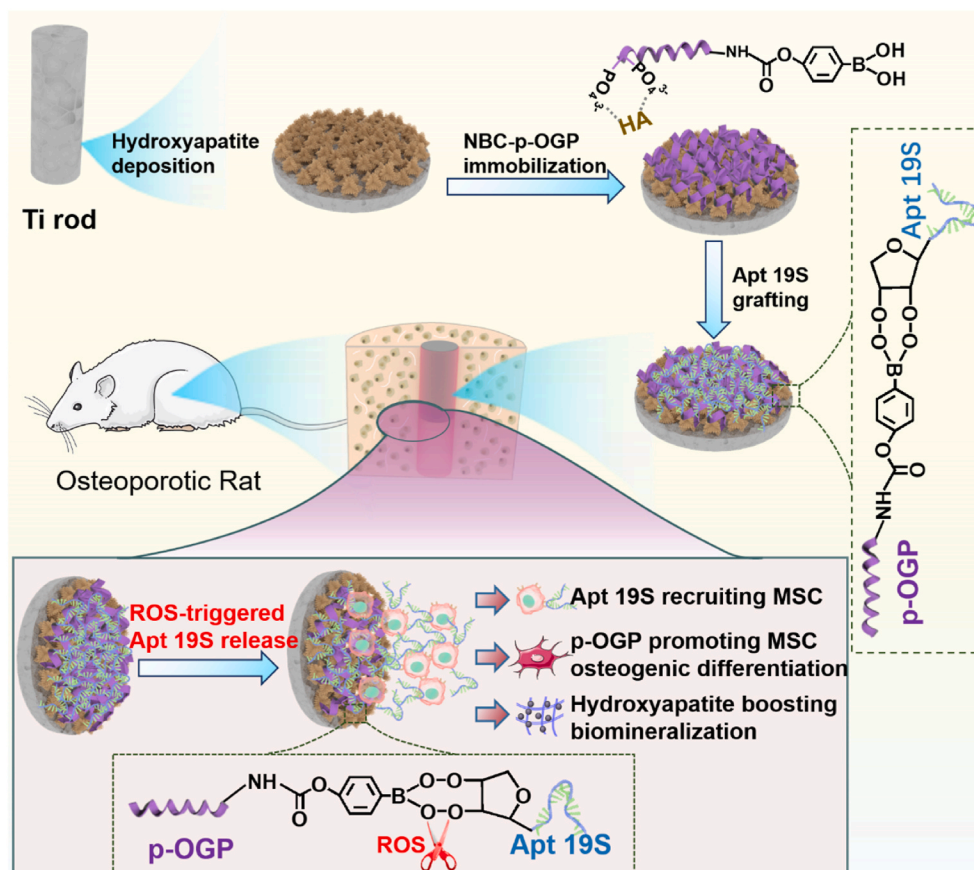
2452-199X/© 2022 The Authors. Publishing services by Elsevier B.V. on behalf of KeAi Communications Co. Ltd. This is an open access article under the CC BY-NC-ND license (<http://creativecommons.org/licenses/by-nc-nd/4.0/>).

early bone repair process.

In osteoporotic condition, the lack of estrogen would up-regulate the reactive oxygen species (ROS) such as  $O_2^-$ ,  $H_2O_2$ ,  $OH^-$ , resulting in rapid accumulation of  $H_2O_2$  in the bone marrow micro-environment, which is the primary site for bone formation through providing biochemical, physical, and mechanical signals for bone related cells [15, 16]. The increasing  $H_2O_2$  level would suppress the differentiation of MSCs and seriously hinder the early bone integration of implants, leading to increasing risk of secondary surgery. At the same time, the amount and activity of MSCs in osteoporotic fracture site are usually insufficient, which may potentially undermine the bone repair efficiency. It's thus necessary to mobilize MSCs from the medullary cavity into the injured site. Many MSC-recruiting strategies have been developed to address this issue. Remarkably, some bioactive molecules that could drive stem cell migration have attracted much attention, such as SDF-1 [17], LL-37 peptide [18] and aptamer (Apt) [19]. Aptamer is a DNA or RNA fragment containing 20–60 base pairs, which has similar specific binding ability like antibodies [20–22]. Apt 19S is a DNA aptamer that can be used to specifically identify pluripotent stem cells, owing to its high affinity with alkaline phosphatase protein on the membrane of bone MSCs that is highly expressed on MSC membrane at all stages [23,24]. Hu et al. developed a double-layer scaffold functionalized with aptamers to capture MSCs [25]. Son et al. proved that combining Apt with hydroxyapatite could promote bone regeneration and angiogenesis [26].

Based on the high ROS level in osteoporotic microenvironment, in this study, we fabricated a ROS-responsive system on titanium surface with hydroxyapatite coating and grafted biomolecules to enhance MSC recruitment and osteogenic differentiation for improving implant osteointegration (Scheme 1). Briefly, the porous hydroxyapatite was introduced onto titanium surface via electrochemical deposition, which

was denoted as Ti/HA. Then, phosphorylated osteogenic growth peptide (*p*-OGP,  $NH_2$ -gly-gly-phe-gly-tyr-leu-thr-arg-gly-gln-arg-lys-leu-ala-T-(Sp)-E-(Tp)-COOH) was synthesized and reacted with 4-nitrophenyl 4-(4, 4, 5, 5-tetramethyl-1,3,2-dioxaborolan-2) benzyl carbonate (NBC) via the amino groups of *p*-OGP with a high conjugation yield of over 85%, which was denoted as NBC-*p*-OGP. After that, NBC-*p*-OGP were immobilized onto Ti/HA surfaces through the binding affinity between phosphate groups of *p*-OGP and calcium on Ti/HA interfaces, which was denoted as Ti/HA/*p*-OGP. Finally, Apt 19S (modified with an RNA molecule at the 3' end) were grafted onto Ti/HA/*p*-OGP implants through the reaction between the boric acid groups of NBC and the dibasic alcohol of Apt 19S. The obtained sample was denoted as Ti/HA/*p*-OGP/Apt. Herein, hydroxyapatite is a commonly used component for titanium modification to enhance biocompatibility and MSC function on account of its structural and elemental resemblance to natural bone. Calcium ion released from degraded hydroxyapatite can also contribute to the osteogenic differentiation [27]. Meanwhile, *p*-OGP is an activator of osteogenic activity and has close relationship to collagen deposition and matrix mineralization [28,29], which can directly regulate the proliferation and differentiation of osteoblasts and mesenchymal stem cells. Previous study confirmed that *p*-OGP can be grafted onto implant surface by covalent bonds and non-covalent interactions to regulate cell behaviors [18] and increase bone formation and trabecular bone density [30]. Apt 19S is the regulatory molecule responsible for MSC recruitment in this study. However, the realization of Apt 19S-mediated MSC recruitment for bone repair requires intricate regulation of its concentration in the implantation site as the MSCs usually move from Apt19S-low to Apt19S-high regions due to the ability of Apt19S to bind with the alkaline phosphatase on MSC surface. Consequently, we have synthesized  $H_2O_2$ -responsive 4-nitrophenyl 4-(4, 4, 5, 5-tetramethyl-1,3,2-dioxaborolan-2) benzyl carbonate (NBC) to anchor the Apt 19S



**Scheme 1.** Construction of bioresponsive functional titanium implant and investigation its effect on local bone remodeling in osteoporosis.

(modified with an RNA molecule at the 3' end) through the reaction between boric acid groups of NBC and the catechol of Apt 19S. Once exposed on the high ROS level, the covalent bond between NBC and Apt 19S was cleaved to regulate the local Apt19S levels for maximized MSC recruitment efficiency. Once MSCs reach the implant interface, their osteogenic differentiation potential would be drastically enhanced by *p*-OGP and hydroxyapatite to facilitate bone regeneration. The study here provided a simple and novel strategy to enhance osteoporotic bone fracture repair via biofunctional titanium implants.

## 2. Materials and method

### 2.1. Materials

Titanium disks (diameter: 15 mm; thickness: 3 mm) and rods (diameter: 1.2 mm; length: 10 mm) were purchased from Northwest Institute for Non-ferrous Metal Research, China. The osteogenic growth peptide modified with two phosphate groups (*p*-OGP, NH<sub>2</sub>-gly-gly-phe-gly-tyr-leu-thr-arg-gly-gln-arg-lys-leu-ala-T-(Sp)-E-(Tp)-COOH) was purchased from Shanghai Xinhao Biological Technology Co., Ltd. Apt 19S were synthesized by Biotechnology (Shanghai) Co. (Chongqing, China). Calcium chloride (CaCl<sub>2</sub>), fluorescein isothiocyanate (FITC), rhodamine and Hoechst 33258 were purchased from Sigma-Aldrich (St. Louis, MO, USA). Other chemicals were provided by Oriental Chemical Co. (Chongqing, China).

### 2.2. Preparation and characterization of surface coating

#### 2.2.1. Synthesis of NBC-*p*-OGP

4-nitrophenyl 4-(4, 4, 5, 5-tetramethyl-1,3,2-dioxaborolan-2) benzyl carbonate (NBC) was synthesized by literature method [31]. Firstly, (hydroxymethyl) phenylboronic acid pinacol ester (0.5 g) was dissolved in anhydrous tetrahydrofuran (THF, 15 mL) under protection of nitrogen at 0 °C. Then, triethylamine/4-(dimethylamino) pyridine (0.6 mL/0.04 g) and 4-nitrophenyl chloroformate (0.47 g) were dissolved in THF (15 mL). The above solution was mixed gently and stirred for 3 h at room temperature. The target products were extracted with saturated sodium chloride and HCl solution (1 M). The organic phase was collected and dried in high vacuum. NBC was purified by passing through silica gel column and eluted with dichloromethane solution containing 40% petroleum ether. White NBC solids were obtained after high vacuum drying. To characterize the NBC linkers, the samples were dissolved in Chloroform-*d* and detected by Bruker Swiss 400 MHz. <sup>1</sup>H NMR (400 MHz, CDCl<sub>3</sub>-*d*): δ (ppm) 1.26 (s, 12H, (CH<sub>3</sub>)<sub>3</sub>), 5.42 (s, 2H, CH<sub>2</sub>), 7.3 (d, 2H, (CH)<sub>2</sub>), 7.45 (d, 2H, (CH)<sub>2</sub>), 7.85 (d, 2H, (CH)<sub>2</sub>), 8.2 (d, 2H, (CH)<sub>2</sub>).

Subsequently, the NBC-*p*-OGP was prepared. Briefly, 14 mg of osteogenic growth peptide modified with two phosphate groups (*p*-OGP) was dissolved in aqueous solution (2.3 mL). DMSO solution (80 μL) containing 5 mg of NBC was then added to the above solution and further stirred at room temperature for 12 h. The target product was purified by dialysis with double distilled H<sub>2</sub>O (ddH<sub>2</sub>O) using dialysis bag (500 D) for one week, then freeze-dried and stored at -20 °C.

Fluorescamine (4-phenylspiro [furan-2(3H), 1'-phthalan]-3, 3'-dione) was used for the quantification of amines groups on *p*-OGP. Fluorescamine (0.3 mg) was dissolved in acetone (1 mL) and *p*-OGP or NBC-*p*-OGP (0.1 mg) was dissolved in deionized water (1 mL). Then the fluorescamine solution was added into 240 μL *p*-OGP or NBC-*p*-OGP solution and incubated 20 min at 37 °C. The fluorescence emission in the range of 460–560 nm was measured at the excitation wavelength of 388 nm by fluorescence spectrophotometer (RF-6000, Shimadzu).

#### 2.2.2. Preparation and characterization of ROS responsive Ti substrate

Titanium disks (diameter: 15 mm; thickness: 3 mm) were polished and cleaned, then washed with mixed acid (HF/HNO<sub>3</sub>/H<sub>2</sub>O:1/3/10) for 5 min to form a rough surface. Afterwards, titanium disks were used as the cathode of electrochemical reaction and platinum as the anode in

electrolyte solution A (CaCl<sub>2</sub>: 0.133 g/L; NH<sub>4</sub>H<sub>2</sub>PO<sub>4</sub>: 0.083 g/L; NaCl: 5.844 g/L) with a constant voltage of 3 V for 1 h at 85 °C. Then the electrolyte solution A was replaced with electrolyte solution B (CaCl<sub>2</sub>: 1.0656 g/L; NH<sub>4</sub>H<sub>2</sub>PO<sub>4</sub>: 0.6624 g/L; NaCl: 5.844 g/L; trisodium citrate: 1.195 g/L) and the reaction was carried out at a constant voltage of 3.4 V for 35 min at 60 °C. Finally, white hydroxyapatite powder was observed on the surface of titanium, denoted as Ti/HA.

NBC-*p*-OGP was grafted on Ti/HA surface via chelation between calcium ion on hydroxyapatite and phosphate group on NBC-*p*-OGP molecules. Briefly, Ti/HA was soaked in 5 mg/mL of NBC-*p*-OGP solution with stirring for 12 h. After washing with distilled water, the obtained samples were denoted as Ti/HA/*p*-OGP, which was further treated with 0.5 mM of Apt 19S solution and stirred for 12 h. The samples were denoted as Ti/HA/*p*-OGP/Apt.

Scanning electron microscopy (SEM), atomic force microscopy (AFM) and water contact angle analysis were used to characterize the surface morphology. X-ray photoelectron spectroscopy (XPS) and transmission electron microscope (TEM) were used to analyze the element composition of different substrates. The copper grid was attached onto the Ti surface before the electrodeposition-enabled preparation of Ti/HA. After formation of HA on the surface of Ti and copper grid, the copper grid was taken out for TEM imaging. The total porosity of the mineral coating was calculated using the following formula: Total porosity = 100% -  $\frac{\rho_B}{\rho_0} \times 100\%$ , where  $\rho_B$  is the bulk density of mineral layer calculated by dividing the total mass with volume ( $\rho_B = 1.56 \text{ mg/mm}^3$ ) while  $\rho_0$  is the density of hydroxyapatite ( $\rho_0 = 3.16 \text{ mg/mm}^3$ ) [32]. Besides, the mechanical properties of different substrates were also measured by TRM100 friction testing machine equipped with load (2 N and 15 N) at a crosshead speed of 70 r/min, which resembles the knee movement. The tribological behaviors were tested under lubrication of PBS at 37 °C. The friction coefficient and cumulative wear mass were directly measured by the machine. The wear rate (W, mm<sup>3</sup>/Nm) was calculated using the following formula.

$$W = \frac{m}{\rho \times N \times S}$$

In this formula, *m* is cumulative wear mass (mg),  $\rho$  is the density of hydroxyapatite ( $\rho = 3.16 \text{ mg/mm}^3$ ), *N* is loading force (15 N), *S* is wear distance (m) in the testing process.

#### 2.2.3. Drug loading capacity of the titanium implant

FITC labeled *p*-OGP was used to monitor the loading of *p*-OGP on titanium surface, and entire operation was carried out in the dark. Briefly, *p*-OGP and FITC were dissolved in PBS (pH 7.8) at a molar ratio of 1:1 with stirring at room temperature for 20 h. After dialysis for 3 days, the target products were denoted as FITC-*p*-OGP. Ti/HA samples have a disk-like shape with a diameter of 15 mm and a thickness of 3 mm, both of which were measured by digital caliper. According to the calculations, the samples have a volume of 0.53 cm<sup>3</sup> and surface area of 1.766 cm<sup>2</sup>. The sample was immersed into FITC-*p*-OGP and washed with PBS for three times and denoted as Ti/HA/*p*-OGP-FITC. Fluorescence microscope (IFM, OLYMPUS IX71, Japan) was used to observe the distribution of *p*-OGP-FITC on the surface of titanium. Fluorescence analysis of FITC-*p*-OGP solution was performed before and after soaking Ti/HA, the optimal concentration of *p*-OGP solution (5 mg/mL) was selected as the standard treatment for the following experiments.

FITC-labeled Apt 19S (purchased from Biotechnology (Shanghai) Co., Ltd, FITC-Apt 19S) was used to study the loading and release behavior of Apt 19S from substrates. Ti/HA was firstly treated with 5 mg/mL of NBC-*p*-OGP as described above. After that, the obtained sample (Ti/HA/*p*-OGP) were immersed into FITC-Apt 19S solution different concentrations (0.1 mM, 0.2 mM, 0.5 mM, 1 mM) with stirring for 24 h at ambient temperature. After rinsing three times with PBS, the obtained sample was Ti/HA/*p*-OGP/Apt-FITC. CLSM was used to observe the distribution of Apt 19S on the substrates. Meantime, the

samples of Ti/HA were immersed into FITC-Apt 19S to detect the un-specific binding between HA and Apt 19S. Nanodrop was used to detect the amount of Apt 19S (single-stranded DNA) before and after soaking, the optimal grafted concentration of Apt 19S was 0.5 mM, which was used to prepare the samples for the following experiments.

#### 2.2.4. The release behavior of Apt 19S from titanium substrates

Ti/HA/p-OGP/Apt was immersed into 1 mL of PBS buffer with or without H<sub>2</sub>O<sub>2</sub> (300 μM) supplementation. 2 μL of the incubation solution was taken out to detect the Apt 19S level by Nanodrop. The incubation solution (2 μL) was taken out at predetermined time points such as 1, 5, 10, 24, 48, 96 h). Meantime, 2 μL fresh PBS with or without H<sub>2</sub>O<sub>2</sub> was added into incubation solution.

#### 2.2.5. The degradation of hydroxyapatite

Ti/HA, Ti/HA/p-OGP and Ti/HA/p-OGP/Apt were immersed into 1 mL PBS buffer with H<sub>2</sub>O<sub>2</sub>. The incubation solution was collected at different time and added with fresh PBS buffer containing H<sub>2</sub>O<sub>2</sub>. The incubation solution was used to detect the content of calcium and phosphorus by inductive coupled plasma emission spectrometer (ICP) and micro tissue inorganic phosphorus content assay kit (solarbio), respectively. During phosphorus detection, the baseline phosphorus level in PBS buffer should be deducted.

### 2.3. Cell culture

MSCs were extracted from bone marrow cavity of Sprague Dawley rat (female, 100 g) under sterile conditions and the associated experimental methods have been reviewed and approved by the Animal Welfare Committee of Chongqing Medical University. The MSCs cultivated with DMEM low-glucose medium (containing 10% FBS), and the culture-medium was replaced every other day. When cell confluence reached 90%, they were detached and reseeded in new culture flasks. The third passage cells were used for all experiments.

### 2.4. In vitro osteogenesis assay

#### 2.4.1. Cell morphology observation

Cells were cultured on Ti, Ti/HA, Ti/HA/p-OGP, Ti/HA/p-OGP/Apt with DMEM containing 300 μM of H<sub>2</sub>O<sub>2</sub>. The initial cell density was  $5 \times 10^3$  cells/cm<sup>2</sup>. After culturing for 24 h, cells on different samples were treated with paraformaldehyde for 30 min and then permeabilized with Triton-X100 for 5 min at room temperature. Thereafter, cell cytoskeleton and nucleus were stained by 5 U/mL of rhodamine-labeled phalloidin (Invitrogen Co.) and 5 μg/mL of Hoechst 33258 (Sigma Aldrich), respectively. Finally, the samples were mounted by 95% glycerin and characterized by a confocal laser scanning microscope (CLSM).

#### 2.4.2. Cell viability assay

MTT assay was used to detect the viability of MSCs cultured on different substrates with an initiated density of  $1 \times 10^4$  cells/cm<sup>2</sup> and the media were changed every two days. Briefly, MSCs were seeded on different substrates supplied with DMEM containing H<sub>2</sub>O<sub>2</sub>. After 3 and 7 days, the medium was discarded and the cells were washed three times with sterile PBS. Then, 400 μL of serum-free medium containing 10% MTT was added to every well and incubated at 37 °C for 4 h. After that, 200 μL of dimethyl sulfoxide (DMSO) solution was used to replace the serum-free medium and shaken at room temperature for 10 min. Finally, the DMSO was transferred to 96-well plates and measured at 490 nm using a microplate reader (Bio-Rad 680).

#### 2.4.3. Alkaline phosphatase (ALP) activity

The MSCs were seeded onto the surface of TCPS, Ti, Ti/HA, Ti/HA/p-OGP, Ti/HA/p-OGP/Apt and the media were changed every two days, respectively. After culturing for 3, 7 and 14 days, cells were lysed by 1% Triton X-100 for 30 min, then the alkaline phosphatase activity and the

total protein concentrations of MSCs were detected according to the instructions of the Alkaline phosphatase assay kit (Nanjing Jiancheng Bioengineering Institute) and BCA Protein Assay Kit (Beyotime), respectively. After that, the optical densities that corresponded to the alkaline phosphatase activity and total protein concentration were measured with microplate reader (Bio-Rad 680) at wavelengths of 490 nm and 595 nm.

#### 2.4.4. Intracellular calcium and phosphorus test

The MSC was cultured on different Ti-based substrates for 7 days. The samples were washed three times with PBS and added 300 μL Hoechst 33258 for staining nucleus. Then 300 μL Fluo-4 AM working solution was added to stain intracellular calcium. After culturing for 30 min at 37 °C, the samples were observed by CLSM.

To quantify the intracellular calcium, MSCs were seeded on different substrates for 7 days. After washing with PBS for three times, the cells were treated by cell lysis buffer for 1–2 s, centrifuged at 10000 g for 5 min at 4 °C to collect the supernatant for quantify intracellular calcium by calcium colorimetric assay kit (beyotime).

MSCs were cultured on different Ti-based substrates for 7 days, then the intracellular phosphorus was detected according to the instruction of the micro tissue inorganic phosphorus content assay kit (solarbio).

#### 2.4.5. Mineralization test

The MSCs were seeded on the different substrates and the media was changed every two days. After 14 days, cells were fixed with 4% paraformaldehyde and stained by alizarin red S (40 mM, pH 4.1). The samples were washed with deionized water and photographed with an optical microscope (MVX10, Olympus). After that, the stained cells were scraped off and washed with 200 μL 10% V/V acetic acid and transferred into 1.5 mL Eppendorf tubes at 85 °C for 10 min. Then, the supernatant containing cells and acetic acid was collected after centrifugation with 10000 r/min. Finally, 10% ammonium hydroxide was added and the absorbance at 450 nm was detected by microplate reader (Bio-Rad 680). The mineralization was calculated according to the formula:

$$\frac{\text{Absorbance}(\text{sample}) - \text{Absorbance}(\text{hydroxyapatite})}{\text{Absorbance}(\text{TCPS})} \times 100\%.$$

#### 2.4.6. Quantitative real-time PCR

mRNA levels associated with osteogenesis (Runx2, Col I, OCN, OPN and OPG) were quantified by qRT-PCR. Briefly, the mRNA of MSCs grown on different substrates were extracted according to the instructions of the RNA extraction kit (Bioteck Coand), of which the first strand cDNA was synthesized by reverse transcription of RNA. Finally, real-time PCR was done on the Bio-Rad CFX Manager system. The amplification conditions of cDNA are: 95 °C for 3 s, followed by 45 cycles at 95 °C for 5 s, and subsequently 60 °C for 30 s.

#### 2.4.7. Western blot analysis

MSCs on different substrate surfaces for 24 h and change the media every two days. Then lysed the cells with RIPA Lysis Buffer and collected the protein-containing supernatant after centrifugation for 5 min at 12000 rpm. After that, proteins were segregated by 10% SDS polyacrylamide and blotted with polyvinylidene fluoride (PVDF) membrane (Millipore). Then, the protein samples were blocked with 5% skimmed milk solution for 2 h before being immersed into solution containing specific primary antibodies for incubation at 4 °C overnight, followed by the treatment with secondary antibodies under room temperature for 1 h. Finally, the samples were analyzed via a luminescent imager. Image analysis was performed using Quantity One (version 4.6.2). The primary antibodies in this study include Runx2, Col I, OCN, OPN, OPG, cdc42, p-FAK/FAK, Vimentin and integrin α5β1 which were originated from rabbit and obtained from Cell Signaling Technology co. ltd. They were diluted by primary antibody dilution buffer (Beyotime co. ltd.) with a ratio of 1:1000. The secondary antibody was anti-rabbit and obtained from Bioss co. ltd, which was diluted with secondary antibody dilution

buffer (Beyotime co. ltd.) with a ratio of 1:5000.

## 2.5. *In vitro* migration evaluation

### 2.5.1. Cell invasion assay

Invasion assay was used to assess the effects of Apt 19S on MSC migration, the initial cell density was  $1 \times 10^4$  cells/cm<sup>2</sup>. Briefly, the transwell chambers (pore size = 8  $\mu$ m, Corning) were placed on a 24-well plate as upper chamber. Ti, Ti/HA, Ti/HA/p-OGP and Ti/HA/p-OGP/Apt were put into bottom chamber. Then 500  $\mu$ L medium with 1% FBS and 100  $\mu$ L serum-free DMEM were added into the bottom chamber and upper chamber, respectively. After culturing for 12, 24 and 36 h, the non-migrated MSCs were removed gently by a cotton swab and the migrated MSCs were immobilized with paraformaldehyde. Finally, migrated MSCs were stained with 0.1% crystal violet solution. Five random areas in every sample were imaged by Olympus inverted microscope and the average of cells number were counted.

### 2.5.2. Gelatin zymogram

The MSC-mediated degradation of extracellular matrix was tested by gelatin zymography. Briefly, the supernatant of culture medium of MSCs was collected after 12 h and 24 h, the protein concentration was measured by BCA kit. The extracted proteins were added into 10% SDS-polyacrylamide gels (contained 1% gelatin). After electrophoresis for 1 h, the gels were washed with 2.5% Triton-X 100 for 3 times and soaked into proteolysis buffer at 37 °C for 16 h. Then, the samples were washed with Triton-X 100 and stained with Coomassie blue solution for 1 h. After treatment with methanol and acetic acid solution for 20 min, the bands could be clearly observed and the gels were imaged to record the MMP activity by Molecular Imager Versa Doc MP 4000 system (Bio-Rad).

### 2.5.3. Wound healing assay

Wound healing assay was used to investigate the mobility of MSCs. Briefly, the third passage stem cells were seeded on TCPS, Ti, Ti/HA, Ti/HA/p-OGP, Ti/HA/p-OGP/Apt, the initial cell density was  $1 \times 10^4$  cells/cm<sup>2</sup>. Then a straight scratch was made via P20 pipette tip when cell confluence reached 90% on different samples. After culturing for 24 h, MSCs were immobilized and stained with rhodamine-phalloidin and Hoechst 33258. Finally, cells in the wound area were observed by CLSM.

## 2.6. *In vivo* study

### 2.6.1. Implantation surgery

The rats were also purchased and housed in Chongqing Medical University and the *in vivo* experiment was carried out strictly following the guidelines of the Animal Welfare Committee of Chongqing Medical University (SYXK-PLA-20120031). After both ovaries have been removed three months, different Ti rods (diameter: 1.2 mm; length: 10 mm) were implanted into the epiphysis of osteoporotic (OVX) rat femur. The whole surgical procedure was done under sterile conditions. Briefly, 4% chloral hydrate sodium was injected into abdominal cavity to narcotize rats. Then a cylindrical defect was created on the epiphysis of femur of OVX rats through surgical drill and different Ti implants were inserted into the defect of the femoral epiphysis. Finally, the incision was sewed up with sutures.

### 2.6.2. X-ray observation and histology analysis

To observe the position of implants in the femoral epiphysis of OVX rats, X-ray imaging was performed at 30 days post surgery. For histology analysis, the femoral epiphysis containing Ti rod was taken out at 3, 7, 30 days after implantation. The samples were fixed with 4% of paraformaldehyde for 48 h before treating with 12% ethylene diamine tetraacetic acid (EDTA) for 4 weeks. Then different Ti implants were removed out from femoral epiphysis and treated with alcohol of graded concentrations. Next, the samples were embedded into paraffin to

prepare the sections with a thickness of 3–5  $\mu$ m. After that, the sections were stained by hematoxylin/eosin (H&E) and immunofluorescence (CD29, CD90) to characterize the newborn bone and MSCs recruitment around the implants (n = 5).

## 2.7. Statistical analysis

The data in current study was analyzed with OriginPro (version 9.0) via student's *t*-test and one-way analysis of variance (ANOVA).  $P < 0.05$  and  $P < 0.01$  were considered statistically significant.

## 3. Results and discussion

### 3.1. Synthesis of NBC-p-OGP

In this study, the synthesis of NBC and NBC-p-OGP was characterized by <sup>1</sup>H NMR and fluorescent amine assay. Fig. S1 A showed the <sup>1</sup>H NMR spectrum of NBC molecule. The characteristic peaks at 8.2, 7.85, 7.45, 7.3, 5.42 and 1.26 ppm corresponded the hydrogen atoms on benzene ring, methylene and methyl groups of NBC molecules, which was consistent with previous literature [31]. Then, NBC molecule was grafted onto p-OGP via the reaction between the ester bond of NBC and the primary amino group of p-OGP. The reaction was confirmed by fluorescamine. It's reasons that the reaction between p-OGP and NBC would eliminate the primary amide for the reaction with fluorescent amine, leading to a lower level of fluorescent intensity. As shown in Fig. S1B, NBC-p-OGP showed significantly reduced fluorescence intensity compared to p-OGP. The result indicated that NBC-p-OGP was successfully synthesized.

### 3.2. Characterization of functionalized titanium substrate

SEM was employed to characterize the surface morphology of different Ti substrates. As shown in Fig. 1A pure Ti displayed a flat and smooth surface. After the electrodeposition, needle-like hydroxyapatite nanostructures were formed on titanium surface (Ti/HA). According to Fig. 1A, the pores were found homogeneously distributed in the mineral coating, which was consistent with the pore distribution in previous reports employing electrochemical deposition technique [33–35]. The eventual porosity of the mineral coating was around 60%. According to the statistical analysis of SEM images, the pore size was in the range of 50–370 nm with an average diameter of around 177 nm. We have detected the element composite of HA on the surface of Ti by energy dispersive X-ray spectroscopy (EDS). The samples showed a Ca/P molar ratio of 1.65 (Figs. S2A and B), which is close to the calculated Ca/P ratio in HA of 1.67 [36,37] and validated our hypothesis that the CaP minerals on the Ti surface by electrolytic deposition was HA. There was no dramatic difference in surface morphology after the treatment of p-OGP and Apt 19S compared to Ti/HA. TEM results further confirmed hydroxyapatite nanostructures with needle-like morphology was formed on titanium substrates (Ti/HA), which were mainly composed of calcium, oxygen and phosphorus (Fig. 1B). After treatment with p-OGP and Apt 19S, nitrogen also appeared on the titanium surface (Fig. 1B). It was ascribed to the amide group of p-OGP and basic group of Apt 19S.

X-ray photoelectron spectroscopy (XPS) was further used to monitor the deposition of hydroxyapatite and functional molecules on titanium surface. Compared to bare Ti substrates, Ca and P elements were observed on Ti/HA, which was attributed to the deposited hydroxyapatite (Ca<sub>10</sub>(PO<sub>4</sub>)<sub>6</sub>(OH)<sub>2</sub>) on titanium surface (Fig. 1D). Ti/HA/p-OGP displayed N1s peaks in its XPS spectrum, which was due to the amide group in p-OGP. After Apt 19S treatment, of P2p peak intensity increased on XPS spectrum of Ti/HA/p-OGP/Apt, which was mainly caused by the large number of phosphate groups on Apt 19S molecules. The above results suggested that functional molecules of p-OGP and Apt were successfully grafted onto hydroxyapatite coated titanium surface. Typically, the atom ratio of Ca and P in Ca<sub>10</sub>(PO<sub>4</sub>)<sub>6</sub>(OH)<sub>2</sub> is around 1.67,

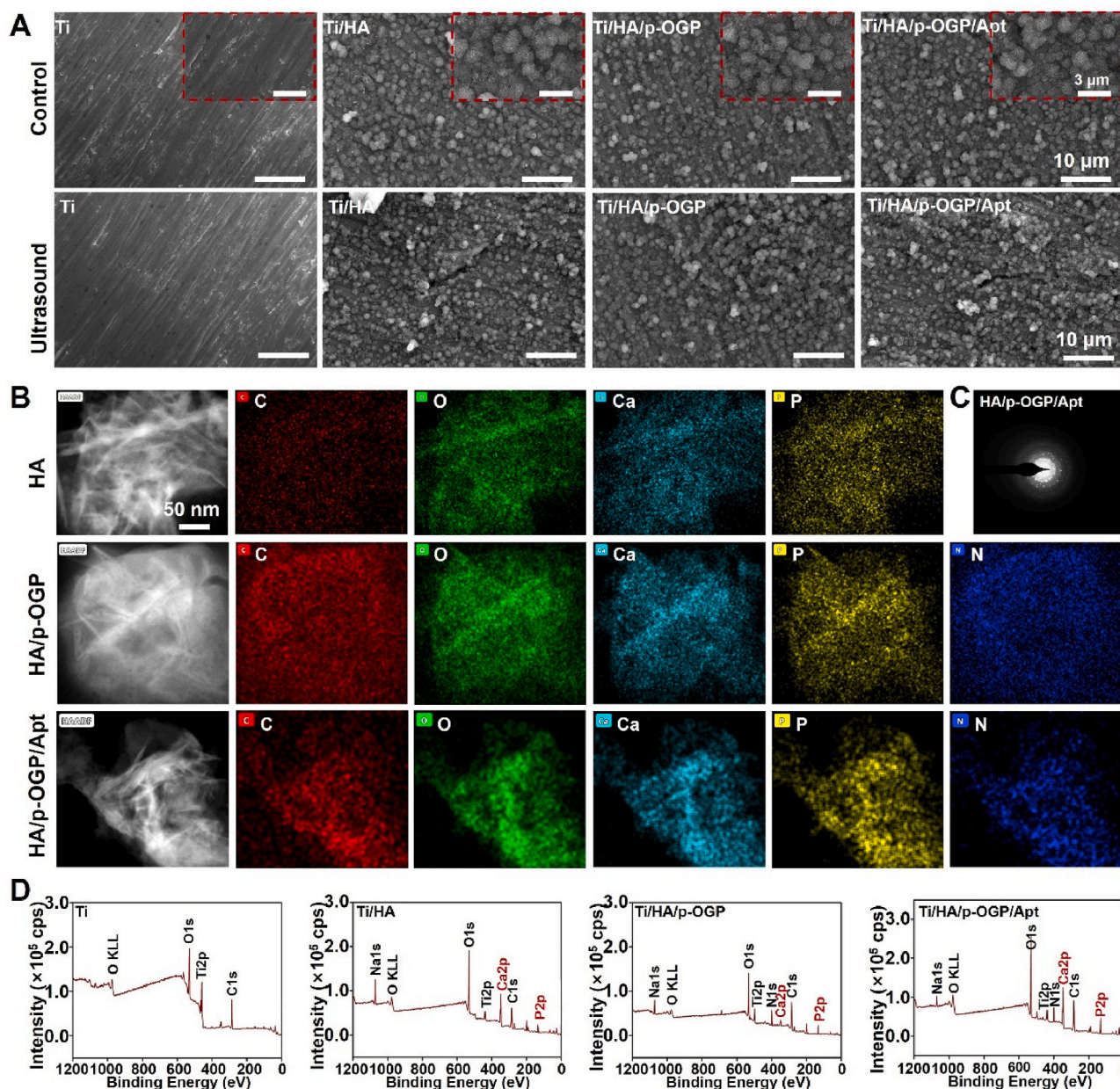
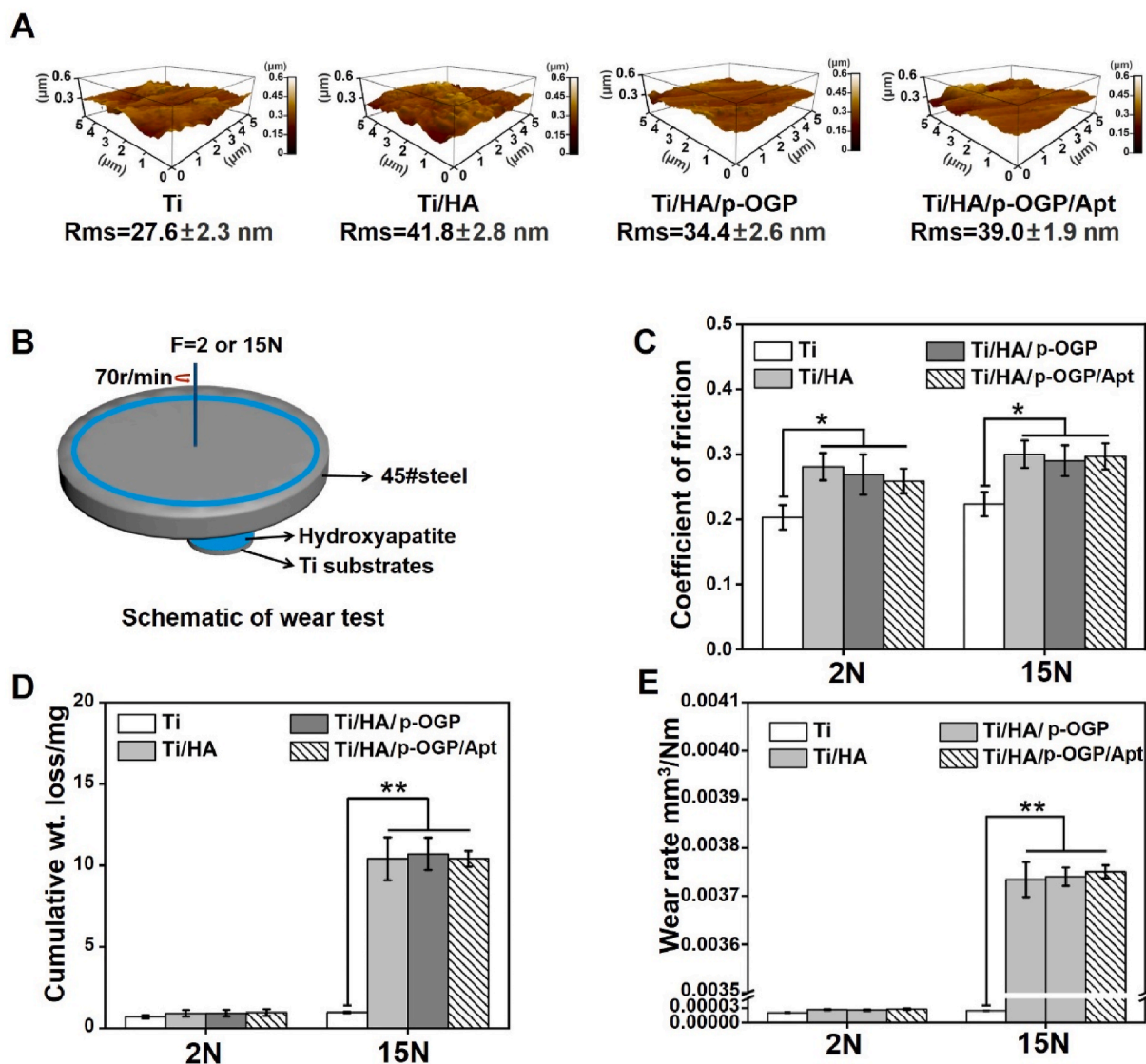


Fig. 1. SEM images and XPS spectra of different substrates. (A) SEM images; (B) TEM images of HA, HA/p-OGP and HA/p-OGP/Apt. (C) Electron diffraction patterns of HA grafted p-OGP and Apt. (D) XPS spectra.

while the Ca/P ratio of HA on the surface of Ti according to the energy dispersive X-ray spectroscopy (EDS) was 1.65, which was highly consistent and confirmed the successful deposition of HA on the titanium surface (Fig. S2C). The EDS data was also supported by the results of the XRD analysis on the crystalline investigations, of which the crystalline peaks were almost identical to the HA-characteristic peaks in the ICDD database. These observations collectively confirmed that HA has been successfully immobilized on the Ti surface by electrolytic deposition. To determine the degradation capability of the HA coating, we have detected the release of Ca and P by inductive coupled plasma emission spectrometer (ICP) and micro inorganic phosphorus content assay kit, of which the results showed that the Ca and phosphate ion levels in the solution would increase gradually, which can be explained by the degradation of hydroxyapatite. As shown in Fig. S2, after 7 days the accumulated released amount of calcium and phosphorus was 5.2  $\mu\text{g}$  and 1.8  $\mu\text{g}$ , respectively. The MSCs could take in calcium and phosphorus from Ti/HA, Ti/HA/p-OGP and Ti/HA/p-OGP/Apt implants,

which is beneficial for biomineralization.

AFM was used to characterize surface roughness of different Ti substrates. As shown in Fig. 2A, Ti/HA displayed a rougher surface with a root mean square (RMS) roughness of 41.8 nm as compared to bare Ti substrate at 27.6 nm. After p-OGP and Apt grafting, the surface roughness of samples slightly decreased to 34.4 nm and 39.0 nm, respectively (Fig. 2A). Previous studies confirmed that the nanostructure with a surface roughness of 30–100 nm was beneficial for the cell growth [38]. The results indicated that hydroxyapatite deposition was the primary cause for the surface roughness changes on Ti substrate. To further investigate the stability of hydroxyapatite on titanium surface, friction testing was carried out with water loading force at 2 N and 15 N and the crosshead speed was 70  $\text{rmin}^{-1}$ , which were consistent with the mechanical stress of implants in the clinics [39]. As shown in Fig. 2C, Ti/HA, Ti/HA/p-OGP and Ti/HA/p-OGP/Apt groups displayed higher ( $P < 0.05$ ) friction coefficient compared to flat Ti surface, which was ascribed to the lower roughness of coating layer compared to other



**Fig. 2.** Physical property characterization. (A) 3D AFM images of different Ti substrates. (B) The cartoon to show the schematic abrasion test process. (C) The coefficient of friction of different substrates. (D) The cumulative weight loss of different substrates, (E) The wear rates of different substrates.

groups. Previous studies have shown that rough surface was beneficial for cell adhesion [40,41]. Furthermore, we have calculated the wear rate (Fig. 2E) of Ti-based substrates according to the cumulative weight loss (Fig. 2D). Specifically, it's well established that the normal load at the femur bone is around 2 N, under which the wear rate of the implant was 0.00007 mm<sup>3</sup>/Nm and within acceptable range. Moreover, when increasing the load to 15 N, the wear rate of the implant increased substantially to 0.0037 mm<sup>3</sup>/Nm and was consistent with the mechanical performance of Ti-based materials in similar reports [42–44]. These results collectively demonstrated that the implant could well resist the mechanical abrasion under normal conditions for a long period, which is beneficial to facilitate its clinical translation. After modification with *p*-OGP and Apt 19S didn't affect the stability of hydroxyapatite (Fig. 2E). The observations were also consistent with previous studies [45]. The results confirmed that hydroxyapatite on titanium has excellent abrasion resistance, which simultaneously avoided the adverse effects of hydroxyapatite shedding on bone tissue. Therefore, Ti/HA/*p*-OGP/Apt had a potential advantage as bone repair implants.

### 3.3. The loading of *p*-OGP and Apt 19S on the titanium

FITC labeled *p*-OGP was used to monitor *p*-OGP loading on Ti/HA. As shown in Fig. S5, the molecular weight of phosphorylated OGP molecules was 2103, which increased slightly to 2492 after the immobilization of FITC molecules. Meanwhile, the FITC-labeled Apt 19S molecules were obtained from Sanggon Biotech. According to the MS provided by the manufacturer, pristine Apt 19S has an average molecular weight of around 15682, while that for the FITC/RNA dual-modified Apt 19S was 16218. These results collectively demonstrated the successful preparation of FITC modification of these biomacromolecules. As shown in Fig. 3A, the green fluorescence intensity of Ti/HA substrate increased along with the *p*-OGP concentration. The Ti/HA substrate displayed the higher level of green fluorescence intensity when the loading concentration of Ti/HA substrate was 5 mg/mL and 10 mg/mL. The green fluorescence intensity with 5 mg/mL was significantly higher than that at 2 mg/mL or 1 mg/mL and there was no significant difference compared to that at 10 mg/mL (Fig. 3A). The results indicated that the optimal grafting concentration of *p*-OGP was 5 mg/mL. The *p*-OGP binding sites might become saturated when its concentration increased above 5 mg/mL considering the insignificant difference in the green

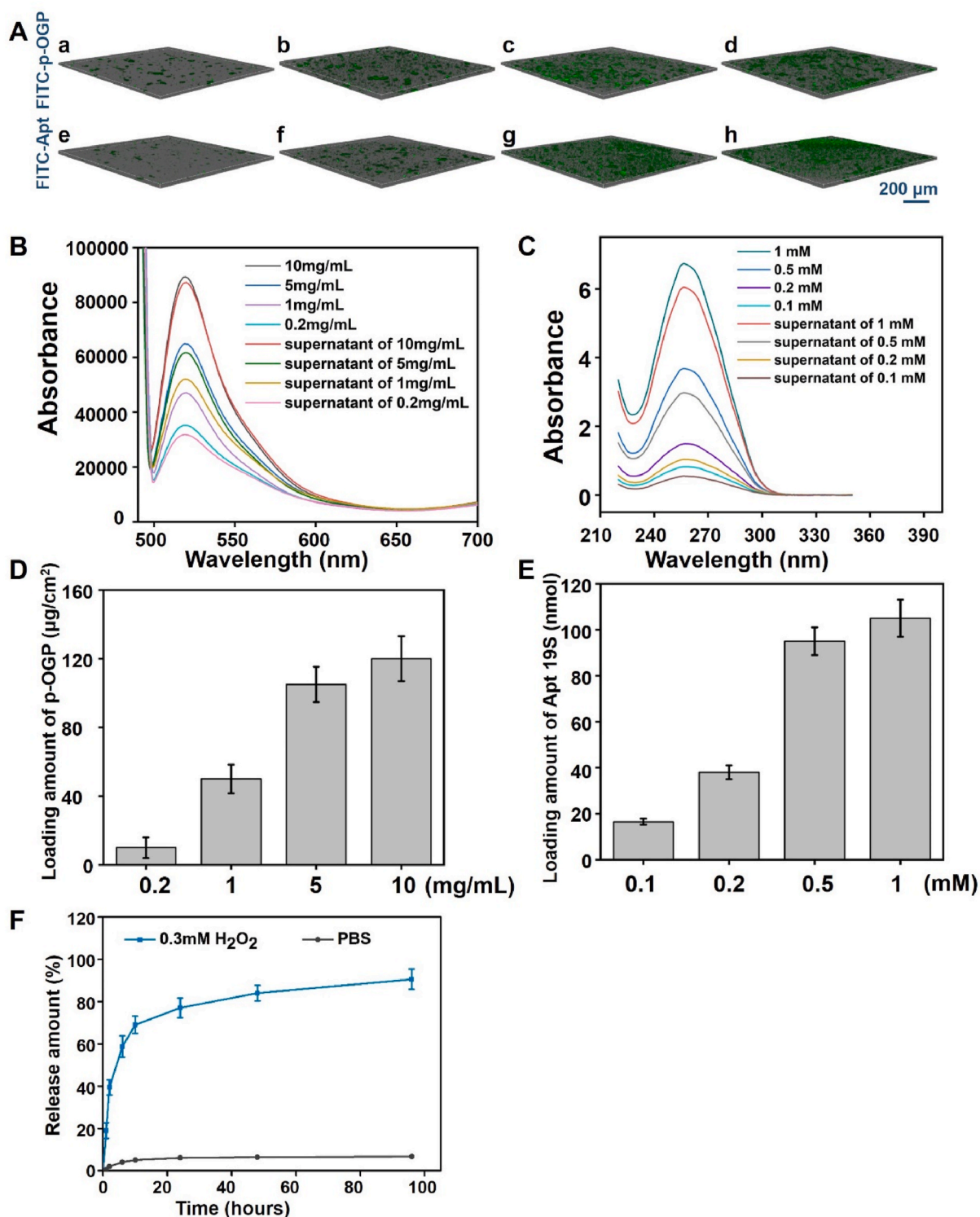


**Fig. 3.** The loading amount of *p*-OGP and Apt 19S in different substrates and the release profiles. (A a-d) Distribution of FITC-*p*-OGP at different concentrations on the surface of the substrate, (a) 0.2 mg/mL, (b) 1 mg/mL, (c) 5 mg/mL, (d) 10 mg/mL; (A e-h) Distribution of FITC-Apt 19S with different concentrations on the surface of the substrate, (e) 0.1 mM, (f) 0.2 mM, (g) 0.5 mM, (h) 1 mM,  $n = 4$ , Scale bar = 200  $\mu\text{m}$ . (B) The fluorescence absorbance of differentiation concentration of FITC-*p*-OGP before and after treatment. (C) The UV absorbance of differentiation concentration of Apt 19S before and after treatment. (D) Quantitative analysis of the loading amount of *p*-OGP. (E) Quantitative analysis of the loading amount of Apt 19S. (F) Apt 19S release profiles from bioresponsive functional interface.

fluorescence between 5 mg/mL and 10 mg/mL. The peptide loading amount per surface area was determined using the following formula:  $\frac{\text{the amount of peptide loading}}{\text{surface area of Ti disks}}$ , which was around 118  $\mu\text{g}/\text{cm}^2$  and confirmed the high drug loading of the implants. (Fig. 3B and D). Next, we also investigate the optimal dose of Apt 19S for the reaction with Ti/HA/*p*-

OGP under a *p*-OGP loading amount of 118  $\mu\text{g}/\text{cm}^2$ . Ti/HA/*p*-OGP displayed obvious higher green fluorescence intensity when Apt 19S was 0.5 mM and 1 mM, but no obvious difference was found between the two loading conditions (Fig. 3 A e-h). Furthermore, the quantitative analysis was performed by nanodrop and showed that the loading amount of Apt

19S was about 98 nmol and 106 nmol at the concentration was 1 mM and 0.5 mM (Fig. 3C and E). The results indicated that the optimal concentration of Apt 19S was 0.5 mM on Ti/HA/p-OGP substrate as the effective loading amount only increased slightly after treating with 1 mM Apt 19S. Based on above studies, 5 mg/mL p-OGP and 0.5 mM Apt 19S were used for fabricating Ti/HA/p-OGP/Apt in the following experiments.

### 3.4. The ROS responsive release behavior of Apt 19S from Ti/HA/p-OGP/Apt

The ROS responsive release behavior of Apt 19S from Ti/HA/p-OGP/Apt was investigated by Nanodrop. As shown in Fig. 3F, Apt 19S was slowly released from Ti/HA/p-OGP/Apt when exposed to PBS buffer without H<sub>2</sub>O<sub>2</sub>. However, a burst release of Apt 19S (78% of the loading amount) from Ti/HA/p-OGP/Apt was observed when incubated in PBS buffer with 300 μM of H<sub>2</sub>O<sub>2</sub> in the first 24 h. In addition, the Apt-characteristic UV absorption in supernatants of Ti/HA group decreased by 23% after incubation for 12 h. It may be caused by un-specific binding between HA and Apt 19S (Fig. S3). The burst release behavior of Apt 19S was caused by the amide bond cleavage under H<sub>2</sub>O<sub>2</sub> condition.

As shown in Fig. 3F, Apt 19S could be efficiently released from the implant surface, for which 76 nmol of Apt 19S was released into the solution medium after 24 h. It could thus be concluded that the H<sub>2</sub>O<sub>2</sub>-triggered Apt 19S release could indeed promote the MSC migration to the implantation site, which was also consistent with the data in Fig. S9C.

### 3.5. Cell migration in vitro

Here we firstly used the transwell chamber to explore the ability of different Ti substrates to recruit stem cells (Fig. 4 A). MSCs were seeded on transwell chamber while functionalized titanium was placed on 24 well plate. Therefore, MSCs would migrate to the lower layer of

transwell chamber due to the bioactive molecules released from Ti substrates. As shown in Fig. 4 B, greater number of cells was observed on the lower layer of transwell chamber after co-incubation with Ti/HA/p-OGP/Apt for 12 h. Nevertheless, Ti/HA/p-OGP/Apt can't induce MSC migration without H<sub>2</sub>O<sub>2</sub> in the medium due to insufficient interaction between Apt 19S and MSC. The trend was more obvious when the time was extended to 24 h. Quantitative analysis further confirmed that Ti/HA/p-OGP/Apt could significantly promote MSC migration as compared to Ti, Ti/HA and even Ti/HA/p-OGP ( $P < 0.01$ ) (Fig. 4C). MSCs from osteoporotic rats showed the same trend (Fig. S7). Meanwhile, gelatin zymography analysis demonstrated that MSCs on Ti/HA/p-OGP/Apt displayed significantly higher secretion level of matrix metalloproteinase 9 (MMP-9) as compared to other groups for 24 h (Fig. 4D).

To further evaluate the effects of different Ti substrates on MSC mobility *in vitro*, wound healing assay was carried out. As shown in Fig. 5A, significant great number of cells migrated into the center of the scratch and formed a new compact cell monolayer for 24 h. However, the amount of cells that migrated to scratch was much lower for bare Ti and Ti/HA substrates. The migration ability of MSCs in the scratch test would be affected by a variety of factors other than the electric potential difference including topological features and hydrophilicity of the implant surface, all of which may retard the migration rates and cause the seemingly low wound healing in the scratch test [46,47]. Consequently, we have extended the incubation period of the scratch test to 36 h and the MSC migration in the Ti/HA group has become more evident compared to the Ti group. We have imaged the scratched area by SEM. As shown in Fig. S4, no apparent damage was observed in the hydroxyapatite coating and consistent with its mechanical resistance in previous sections.

Finally, we evaluated the expression level of migration related proteins including cell division cycle 42 (Cdc42), integrin focal adhesion kinase (FAK) and vimentin in MSCs on different substrates via WB assay. As shown in Fig. 5B, Ti/HA/p-OGP/Apt group significantly improved the protein expression levels of Cdc42, p-FAK/FAK, integrin α5 and

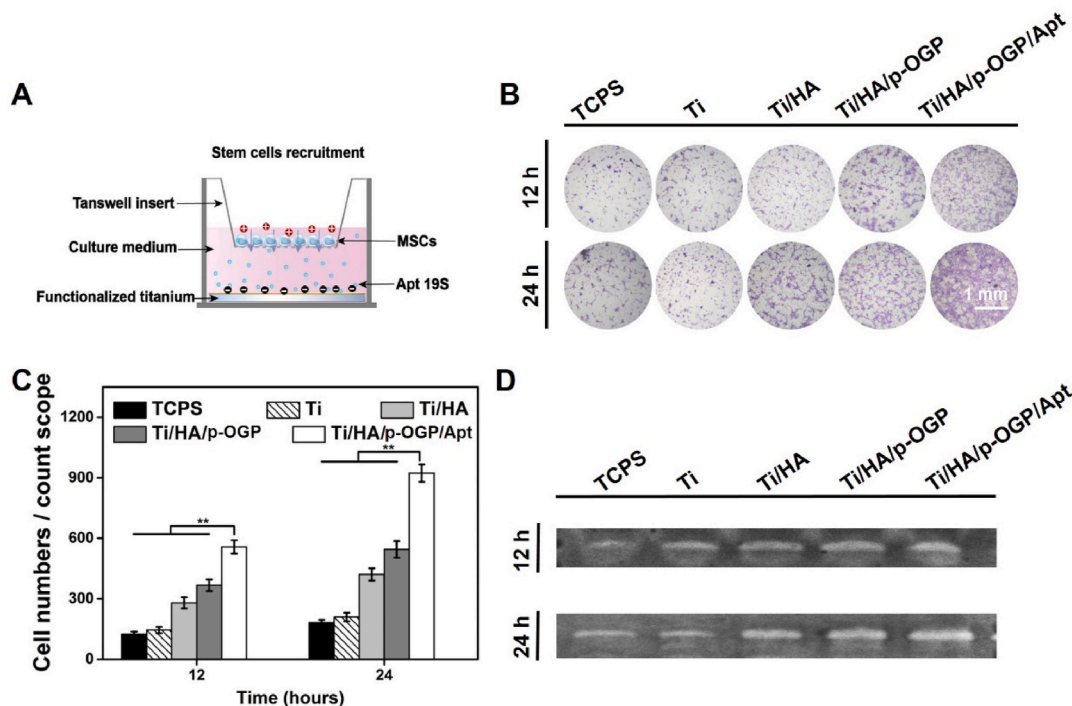
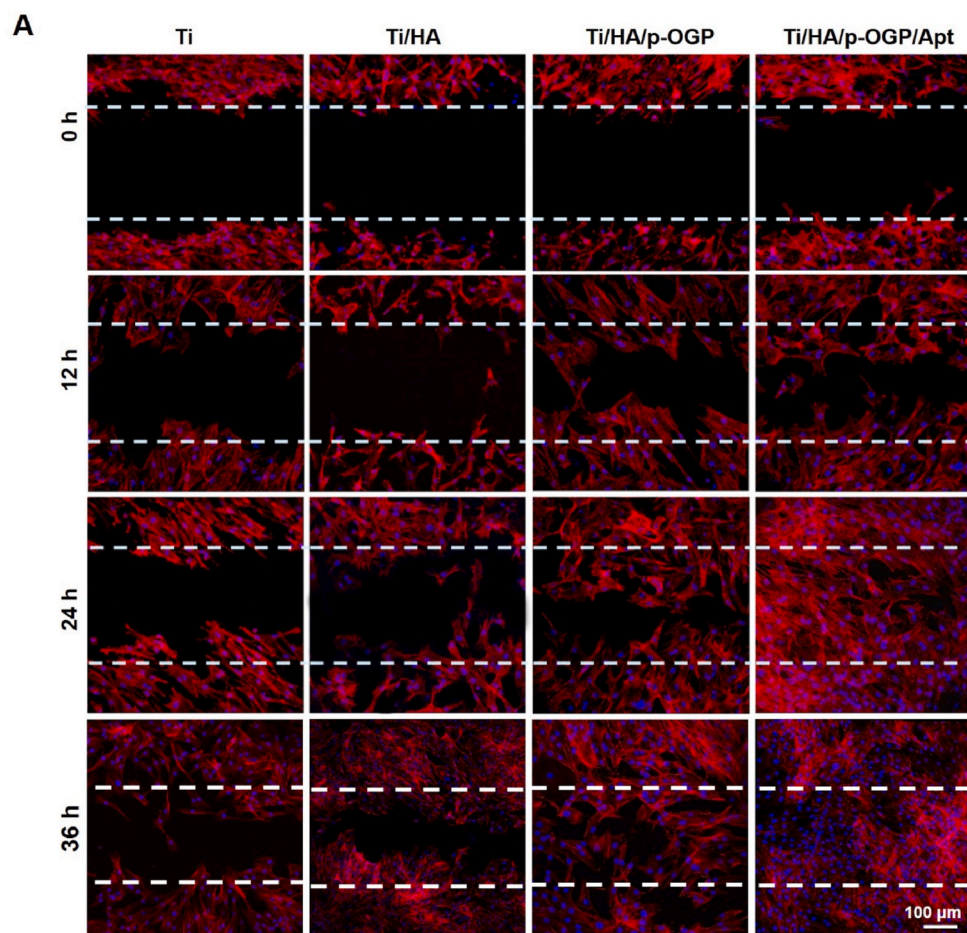
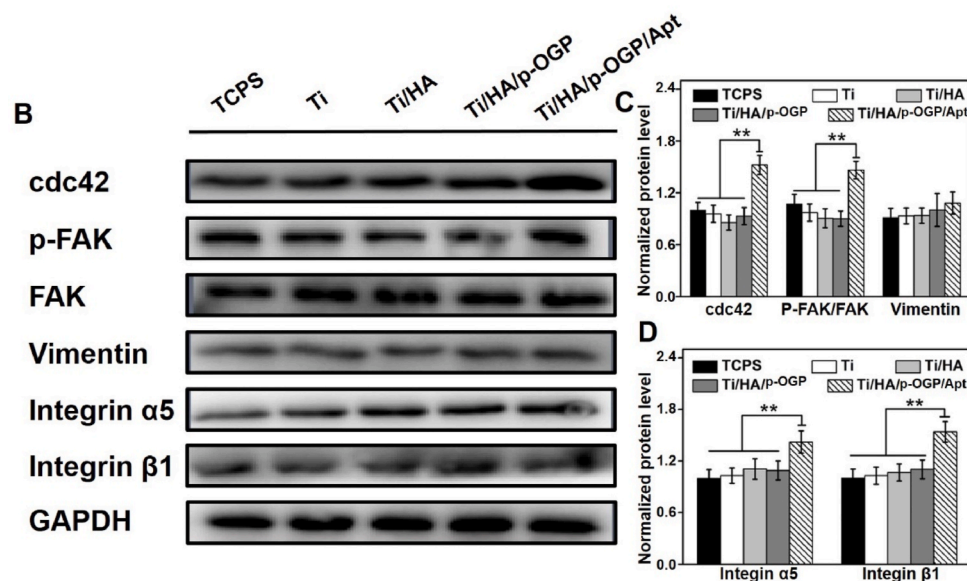


Fig. 4. Transwell and gelatinase spectra of MSCs: (A) Scheme of responsive functional substrate affecting MSCs transmembrane migration; (B) Image of different materials affecting MSCs transmembrane migration; (C) Quantitative analysis of different materials affecting MSCs transmembrane migration,  $n = 6$ ,  $*p < 0.05$ ,  $**p < 0.01$ ; (D) Image of gelatinase spectra of cells cultured for 12 and 24 h.



**Fig. 5.** CLSM images of MSC migration and expression of migration related protein. (A) CLSM images of MSCs for 0, 12, 24 and 36 h culture after scratch. The actin filaments (red) and cell nuclei (blue) were stained individually. (B) Western blot bands of migration related proteins after 24 h of cell culture; (C) Quantitative analysis of the *cdc42*, *p-FAK/FAK*, Vimentin and integrin  $\alpha5$  and integrin  $\beta1$ ,  $n = 6$ ,  $**p < 0.01$ . (For interpretation of the references to color in this figure legend, the reader is referred to the Web version of this article.)



integrin  $\beta1$  in MSCs as compared to other groups. Quantitative analysis also demonstrated that the corresponding protein expression levels in MSCs on Ti/HA/p-OGP/Apt were 1.62, 1.56, 1.27 and 1.46 times higher than that of bare Ti substrate, respectively (Fig. 5C and D). The Ti/HA/p-OGP/Apt implants could promote MSC migration through the combined action of Apt-mediated chemotaxis and HA/p-OGP-mediated galvanotaxis. Specifically, Fig. 5B describes the expression of proteins related to chemotaxis. Due to the lack of Apt component that was critical for

driving the chemotaxis process, it's reasonable that the Ti/HA/p-OGP group wouldn't show significant expression of chemotaxis-related proteins. The cell proliferation of MSCs were detected at 0, 12, 24, 36 h, as shown in Fig. S4B, cells in all groups have showed similar levels of proliferation at all time points with no significant difference, while the *in vitro* scratch tests showed that the MSC number in the scratch area in the Ti/HA/p-OGP/Apt group has increased significantly compared to the other groups, which evidently confirmed the coating-enhanced MSC

migration. On the other hand, Figs. 6B and S9A showed that Apt19S has no promotional effect on MSC proliferation, while Fig. 5B showed that the expression levels of chemotaxis-related proteins have increased significantly in MSCs of the Ti/HA/p-OGP/Apt group. These results collectively demonstrated that the chemotaxis-mediated MSC recruitment was the primary contributing factor for the wound healing effects.

In our study, MSC migration was closely related with Apt 19S released from Ti/HA/p-OGP/Apt substrate. The borate bond between Apt 19S and NBC-p-OGP could be cleaved in a responsive manner when Ti/HA/p-OGP/Apt was exposed to H<sub>2</sub>O<sub>2</sub>, leading to a rapid accumulation of Apt 19S around Ti/HA/p-OGP/Apt substrates within a short period (Fig. 3C). Previous studies have demonstrated that Apt19S has high binding affinity to the MSCs by binding to the alkaline phosphatase overexpressed on MSC membrane. Consequently, a key design in this study is to create a calibrated negative Apt19S gradient from the implant surface, which should stimulate the migration of MSCs from low to high Apt19S concentrations. To realize such a design, the Apt19S molecules were anchored into the mineral coating via H<sub>2</sub>O<sub>2</sub>-responsive NBC linkers, which could be liberated in response to the elevated H<sub>2</sub>O<sub>2</sub> levels

in osteoporotic environment and gradually spread to the surrounding space through diffusion to drive MSC migration. During the migration process, MSCs showed increasing expression levels of related proteins such as MMP, cdc42, p-FAK/FAK and integrin. MMP 9 can expose the arginine-glycine-aspartic acid (RGD) in the extracellular matrix by degrading gelatin. The amount of exposed RGD sequences in extracellular matrix was positively correlated to the expression level of integrin in MSCs. Cdc42 regulates the aggregation of actin and forms microfilaments to promote the formation of pseudopodia [48,49]. As a bridge between extracellular matrix (ECM) and actin, integrin responds to the stimulation from ECM and provides a driving force for cell migration [50,51]. FAK activated (phosphorylation of Tyr<sup>397</sup>) by integrin promotes the transduction of extracellular matrix, which facilitates the anchoring of the cells and affects their movement and migration [52,53]. The dynamic properties of vimentin can also guide the flexibility of cells [54]. Our results indicated that Ti/HA/p-OGP/Apt have higher level expression of MMP9, cdc42, p-FAK/FAK and integrin  $\alpha$ 5 $\beta$ 1, which in turn promoted MSC migration.

Ti/HA and Ti/HA/p-OGP promoted MSCs migration was a

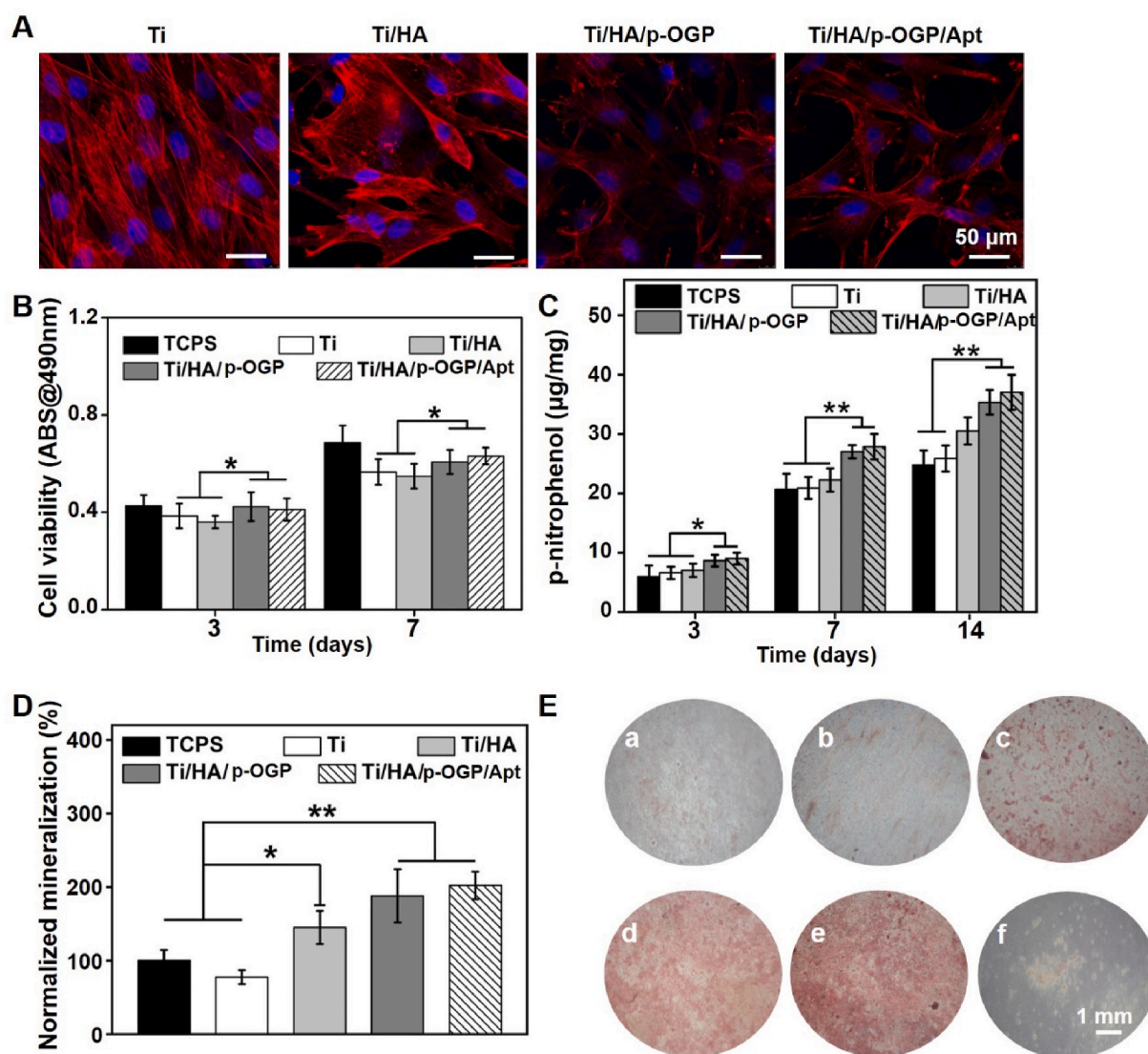


Fig. 6. Morphological characterization, proliferation, alkaline phosphatase activity and mineralization of cells on different materials. (A) CLSM after 24 h of cell culture,  $n = 4$ , scale bar = 50  $\mu$ m. (B) MTT after 3 and 7 days of cell culture. (C) ALP activity after 3, 7 and 14 days of cell culture; (D) Quantitative mineralization after 14 days of cell culture, (E) Alizarin red staining after 14 days of cell culture, (a) TCPS, (b)Ti, (c)Ti/HA, (d)Ti/HA/p-OGP, (e)Ti/HA/p-OGP/Apt, (f) Ti/HA without cells,  $n = 4$ ,  $*p < 0.05$ ,  $**p < 0.01$ , scale bar = 1 mm. (For interpretation of the references to color in this figure legend, the reader is referred to the Web version of this article.)

galvanotaxis process. Specifically, it was well-established that HA is a biomaterial with negative zeta potential, while the electric potential of MSCs membrane was positive in the outer surface but negative in the inner surface. The *p*-OGP molecules have an isoelectric point (PI) of 9.99, while the physiological pH is significantly lower than the PI of *p*-OGP. Consequently, it's anticipated that *p*-OGP molecules would scavenge the protons in the solution environment and cause a significant decrease in the zeta potential of the peri-implant region. Considering the charge status of the MSCs membrane, this would cause a significant electric potential difference between the implant and the MSCs. The exposure of the MSCs to the electric field would asymmetrically open the voltage-gated ion channels and cause the infusion of large amounts of ions, eventually leading to the polarization of the MSCs and activating those associated signaling pathways including PI3K/AKT and PTEN [55, 56]. These effects would induce the MSCs to migrate along the electric field line and enrich on the implant surface. As shown in Fig. S6, the galvanotaxis-related protein expression was increased in the group of Ti, Ti/HA and Ti/HA/*p*-OGP.

### 3.6. Cell viability and osteogenic differentiation in vitro

MSC morphology on different Ti surfaces was observed by CLSM after 24 h incubation. As shown in Fig. 6A, MSCs on both Ti/HA/*p*-OGP and Ti/HA/*p*-OGP/Apt showed better spreading ability and lateral expansion than those of other groups. Meantime, cell viability assay result displayed that both Ti/HA/*p*-OGP and Ti/HA/*p*-OGP/Apt significantly improved MSC activity compared to those of bare Ti and Ti/HA after incubation for 3 and 7 days (Fig. 6B). The results indicated that Ti/

HA/*p*-OGP/Apt has good compatibility *in vitro*.

Next, the intracellular calcium and phosphorus levels were detected. As shown in Fig. S11, MSCs cultured on Ti/HA, Ti/HA/*p*-OGP and Ti/HA/*p*-OGP/Apt displayed higher levels of intracellular calcium and phosphorus after 7 days. The underlying mechanism is that the degradation products of hydroxyapatite were taken in by MSC, which is beneficial for promoting biomineralization. Finally, the osteoblastic differentiation potential of MSCs on different substrates were evaluated by ALP activity and cellular mineralization capacity assay. As shown in Fig. 6C, Ti/HA/*p*-OGP and Ti/HA/*p*-OGP/Apt culture. The trend was more obvious as the time was extended to 7 and 14 days. Furthermore, the mineralization capacity of MSCs on Ti/HA/*p*-OGP and Ti/HA/*p*-OGP/Apt was nearly 2.5-fold higher than that of bare Ti substrate (Fig. 6D). ALP activity was the biomarker of the early osteogenic differentiation of bone repair, which would usually increase rapidly in the early stage of osteogenic differentiation. The obvious mineralized nodules (marked by red color) were observed in Ti/HA/*p*-OGP and Ti/HA/*p*-OGP/Apt (Fig. 6E). The results indicated that introduction of bioactive molecules including *p*-OGP and Apt on Ti substrate was beneficial for the osteoblastic differentiation of MSCs. The existence of H<sub>2</sub>O<sub>2</sub> would suppress the osteogenic differentiation capability of rat bone marrow MSCs, which may contribute to the absence of alizarin red color in the images.

Western blot and qPCR were used to further detect the effect of different Ti substrates on osteoblastic differentiation of MSCs at molecular levels. Runx2 is not only an early marker of osteogenic differentiation but also could act as a transcription factor to stimulate osteogenic differentiation-related proteins (such as OCN, OPN), which is usually highly expressed throughout the osteogenic differentiation

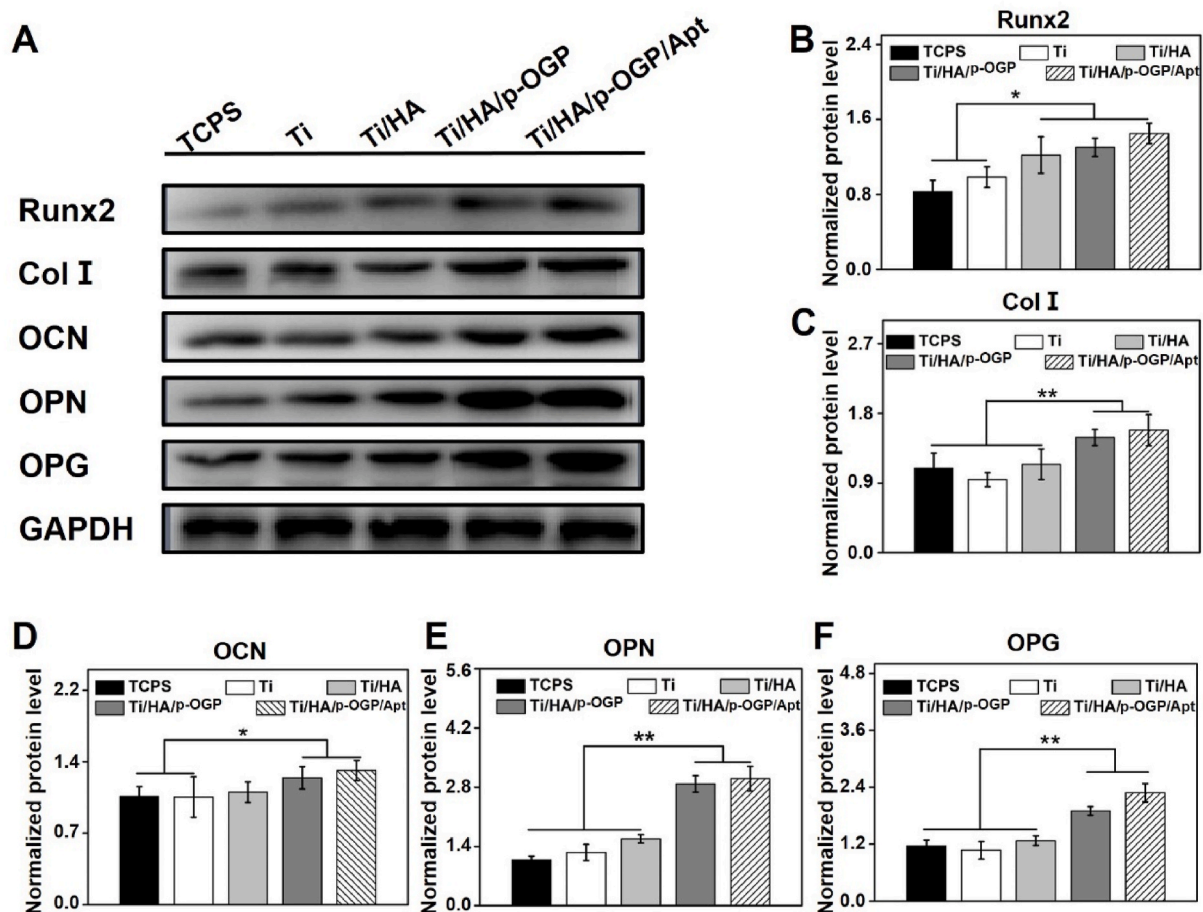


Fig. 7. Expression of osteoblast related protein. (A) Representative western blotting analysis and quantitative analysis of Runx2(B), Col-I (C), OCN(D), OPN(E) and OPG (F) proteins. n = 3, \*p < 0.05, \*\*p < 0.01.

process [57,58]. We have measured the mRNA and protein expression levels of Runx2 in MSCs after culturing for 3- and 7-days on different Ti-based substrates, which have both increased significantly (Figs. S10 and 7A). By referring to the protocols established in previous reports [59,60], we also detected the expression levels of Col I, OCN, OPN and OPG in different groups after 7 days of incubation, which are the important indicators of osteogenic differentiation and closely related to the mineralization of extracellular matrix [61,62]. As shown in Fig. 7A, MSCs on Ti/HA/p-OGP/Apt groups showed the highest expression levels of osteogenic related proteins, followed by Ti/HA/p-OGP and Ti/HA. Compared with Ti group, Ti/HA/p-OGP/Apt increased the protein expression of Runx2, Col I, OCN, OPN, OPG by 1.2 times, 1.85 times, 1.26 times, 2.26 times, 1.76 times at 7 days, respectively (Fig. 7B–F).

MSCs cultured on Ti/HA/p-OGP/Apt showed the highest osteoblastic differentiation level, which was related to p-OGP and hydroxyapatite. The C-terminal pentapeptide of p-OGP is the physiological active form of p-OGP. It can not only improve the proliferation and differentiation ability of osteoblasts and MSCs *in vitro*, but also accelerate the bone formation and enhance trabecular bone density *in vivo* [63]. Meanwhile, hydroxyapatite is structurally and chemically resembling to natural bones and its degradation products are primarily calcium ions and phosphate ions that could participate the formation of new bone apatite [64,65]. In this study, p-OGP boosted the expression of osteogenic differentiation-related proteins and increased the collagen I expression in extracellular matrix. Then, the calcium ions and phosphate ions from hydroxyapatite were assembled into amorphous calcium phosphate (ACP) in endoplasmic reticulum. After that ACP was transformed to extracellular compartment through lysosomal pathway. The combination of ACP and collagen could promote the formation of mineralized extracellular matrix. Herein, Once MSCs are adhered onto Ti substrate under the guidance of Apt 19S, p-OGP and hydroxyapatite synergistically promoted the osteoblastic differentiation of MSCs.

The promotional effect of the Ti/HA/p-OGP/Apt implants on MSC migration and differentiation was further evaluated on MSCs extracted from osteoporotic rats (OP-MSCs), of which the results revealed an almost identical trends and consistently validated the pro-healing benefit of the Ti/HA/p-OGP/Apt implants. Nevertheless, it's also noted that the corresponding values in the OP-MSC-based tests were lower than that on normal MSCs, which could be explained by the osteoporosis-induced inhibition of MSC activities and also consistent with the observations in previous reports [66–68].

### 3.7. MSC recruitment and new bone formation *in vivo*

As shown in Fig. S13, we have constructed osteoporotic rat through removing both ovaries, the quantitative results show that the epiphysis of osteoporotic rats has significantly lower bone volume per total volume (BV/TV), trabecular thickness (Tb. Th), trabecular number (Tb. N) compared to the control group while the trabecular bone pattern factor (Tb.Pf) and trabecular separation (Tb.Sp) have increased, which is in accordance with the typical osteoporosis-associated bone features in recent reports [69,70]. Different Ti rods were implanted into osteoporotic rat to investigate their effects on promoting new bone formation at implant interface. X-ray detection demonstrated that the implant was located at the distal end of the femur and no defect or inflammatory reaction were found around the Ti/HA/p-OGP/Apt implant interface, suggesting that Ti/HA/p-OGP/Apt implants had good histocompatibility. As shown in Fig. S12, the expression levels of TNF- $\alpha$  and IL-6 at the wound area in all groups increased to a high level at 3 days post implantation but decreased steadily afterwards, which eventually dropped to physiological levels at 30 days post implantation. The transient increase in TNF- $\alpha$  and IL-6 levels could be explained by the acute immunological response of the rats after the implantation of foreign objects and confirmed the low inflammation-inducing ability of the implant.

To monitor the MSC recruitment on implant interface, immunohistochemical staining (CD29/CD90 labeled MSCs) were performed after

implantation for 3 days, 7 days and 30 days, respectively. As shown in Fig. 8A, the yellow fluorescence was due to the overlapping of green (originated from the CD29 proteins) and red (originated from the CD90 proteins) colors, both of which are located on the surface of MSCs. Typically, Apt 19S could be completely released from the implant within 7 days according to the release profiles in Fig. 3F, during this period the MSCs would continuously migrate to the injured site and adhere to the implant surface, eventually differentiate into osteoblasts under the influence of both HA and p-OGP within 30 days. The yellow fluorescence intensity was used for reflecting the amount of MSCs in Fig. 8A, which supported the visual trends shown by Fig. 8C and collectively confirmed that only small amount of MSCs have migrated to the implanted site in the group of Ti, Ti/HA and Ti/HA/p-OGP after implantation for 3 days. In contrast, the amount of peri-implant MSCs in the Ti/HA/p-OGP/Apt group has increased by 3 times than the control groups at 3 days. Moreover, the amount of MSCs in the Ti/HA/p-OGP/Apt group showed a steadily increasing trends and was 4 times higher than the control group at 7 days post implantation (Fig. 8C). After implantation for 30 days, the MSC signal decreased greatly in all groups because they have differentiated into osteoblasts. The changes in the amount of peri-implant MSCs were also consistent with the results in Fig. 8B. At the same time, the new bone thickness around the implants at 30 days was quantified for comparison. Previous studies confirm that both CD29 and CD90 are expressed on the surface of MSCs but not the fully differentiated osteoblast, which could explain the disappearance of yellow fluorescence at the implantation site [71,72]. The results indicated that Ti/HA/p-OGP/Apt could effectively recruit MSCs to bone-implant interface for the bone regeneration that followed.

Finally, we evaluated the new bone formation at bone-implant interface via hematoxylin/eosin (H&E) staining. As shown in Fig. 8B, after 3 days of implantation, large number of inflammation-related cells appeared at the site of bone injury in all groups. After 7 days of implantation, it was observed that the amount of newly-formed fibrous bone like tissues was evidently higher in the Ti/HA/p-OGP/Apt group than the others. When the incubation time was extended to 30 days, the new bone formation at the implant-bone interface in the Ti/HA/p-OGP/Apt group was significantly higher than the other groups.

Estrogen deficiency is a hallmark of osteoporosis, which can up-regulate ROS levels and enhance H<sub>2</sub>O<sub>2</sub> accumulation in the bone marrow microenvironment. Once Ti/HA/p-OGP/Apt was implanted into osteoporotic rats, the higher ROS level triggered complete Apt 19S release from the implant within 7 days according to the release profiles in Fig. 3F, during this period the MSCs would continuously migrate to the injured site and adhere to the implant surface, eventually differentiate into osteoblasts under the influence of both HA and p-OGP within 30 days. Importantly, previous studies confirm that both CD29 and CD90 are expressed on the surface of MSCs but not the fully differentiated osteoblast, which could explain the disappearance of yellow fluorescence at the implantation site (Fig. 8A). In addition, p-OGP and hydroxyapatite on Ti/HA/p-OGP/Apt interface synergistically enhanced the osteogenic differentiation of MSCs, leading to increased new bone formation at the implant interface as compared to other groups after implanting 30 days (Fig. 8B).

## 4. Conclusion

In this study, we fabricated a ROS responsive release system on titanium substrates (Ti/HA/p-OGP/Apt) via hydroxyapatite coating and covalent linking with biomolecules. Under higher ROS levels, Ti/HA/p-OGP/Apt could release Apt 19s in response to the surrounding micro-environment, which effectively promoted MSC migration. When implanted into osteoporotic rat, Ti/HA/p-OGP/Apt displayed superiority MSC recruiting capacity and promoted new bone formation after 30 days. Therefore, the study herein provided a simple and effective method to prepare functionalized titanium-based implant for osteoporotic bone repair.

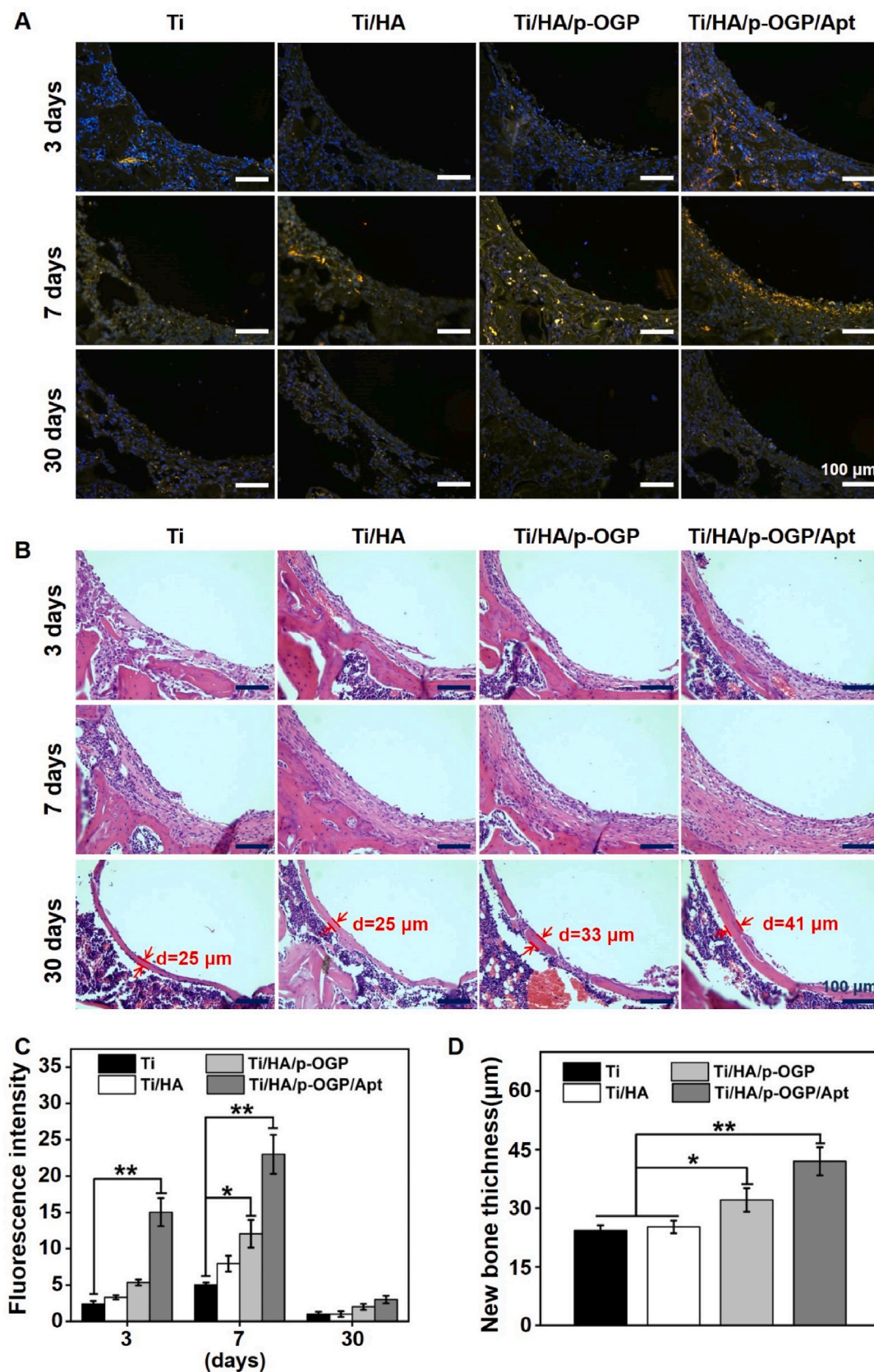


**Fig. 8.** Histological and immunohistochemical staining of the bio-implant interface. (A) Immunofluorescence of CD29/CD90 labeled MSCs at the bio-implant interface at 3, 7 and 30 days after the implantation, MSCs are labeled with yellow fluorescence. (B) H&E staining of the bio-implant interface at 3, 7 and 30 days after the implantation. n = 6, Scale bar = 100 μm. (C) Quantitative analysis of immunofluorescence staining of the bio-implant interface. (D) The new bone thickness around the implants after implantation 30 days. (For interpretation of the references to color in this figure legend, the reader is referred to the Web version of this article.)

## CRedit authorship contribution statement

**Maohua Chen:** Data curation, Formal analysis, Writing – original draft, Writing – review & editing. **Yuting Sun:** 30% data curation. **Yanhua Hou:** Formal analysis. **Zhong Luo:** Conceptualization, Formal analysis, Funding acquisition, Supervision, Writing – review & editing. **Menghuan Li:** Formal analysis, Funding acquisition, Writing – review & editing. **Yujia Wei:** Materials preparation. **Maowen Chen:** Materials characterization. **Lu Tan:** Writing – review & editing. **Kaiyong Cai:** Conceptualization, Formal analysis, Funding acquisition, Supervision, Writing – review & editing. **Yan Hu:** Conceptualization, Data curation, Formal analysis, Funding acquisition, Supervision, Writing – original draft, Writing – review & editing.

## Declaration of competing interest

The authors declare no conflict of interest.

## Acknowledgements

This work was financially supported by National Natural Science Foundation of China (51773023, 21734002, 51825302), National Key R&D Program of China (2017YFB0702603), Graduate Research and Innovation Foundation of Chongqing (CYB20071), Natural Science Foundation of Chongqing Municipal Government (cstc2018jcyjAX0368, cstc2020jcyj-msxmX0834), Returning Overseas Scholar Innovation Program (CX2018062) and Chongqing Outstanding Young Talent Supporting Program (CQYC201905072), Fundamental Research Funds for the Central Universities (2019CDQYSW005, 2020CDJQY-A075, 2020CDJYJZL009).

## Appendix A. Supplementary data

Supplementary data to this article can be found online at <https://doi.org/10.1016/j.bioactmat.2022.02.006>.

## References

- R. Wang, M. Shi, F.Y. Xu, Y. Qiu, P. Zhang, K.L. Shen, Q. Zhao, J.G. Yu, Y.F. Zhang, Graphdiyne-modified TiO<sub>2</sub> nanofibers with osteoinductive and enhanced photocatalytic antibacterial activities to prevent implant infection, *Nat. Commun.* 11 (2020) 4465.
- B.L. Tao, W.K. Zhao, C.C. Lin, Z. Yuan, Y. He, L. Lu, M.W. Chen, Y. Ding, Y.L. Yang, Z.Z.L. Xia, K.Y. Cai, Near infrared light-triggered on-demand Cur release from Gel-PDA@Cur composite hydrogel for antibacterial wound healing, *Chem. Eng. J.* 390 (2020), 124621.
- J.C.M. Souza, M.B. Sordi, M. Kanazawa, S. Ravindran, B. Henriques, F.S. Silva, C. Aparicio, L.F. Cooper, Nano-scale modification of titanium implant surfaces to enhance osseointegration, *Acta Biomater.* 8 (2019) 112–131.
- L. Kyloenen, M. D'Este, M. Alini, D. Eglin, Local drug delivery for enhancing fracture healing in osteoporotic bone, *Acta Biomater.* 11 (2015) 412–434.
- Z. Wang, Y. Niu, X. Tian, N. Yu, C. Wang, Osseointegration: switching on and off macrophages by a "bridge-burning" coating improves bone implant integration under osteoporosis, *3D Print.* 31, 2021, 2170043.
- J.J. Tian, R. Shi, Z. Liu, H. Ouyang, M. Yu, C.C. Zhao, Y. Zou, D.J. Jiang, J.S. Zhang, Z. Li, Self-powered implantable electrical stimulator for osteoblasts' proliferation and differentiation, *Nano Energy* 59 (2019) 705–714.
- B. Li, X. He, Z. Dong, Ionomycin ameliorates hypophosphatasia via rescuing alkaline phosphatase deficiency-mediated L-type Ca<sup>2+</sup> channel internalization in mesenchymal stem cells, *Bone Res* 8 (2020) 19.
- S. Wasnik, R. Lakhani, D.J. Baylink, C.H. Rundie, Y. Xu, J. Zhang, X. Qin, K.W. Lau, E.E. Carreon, X. Tang, Cyclooxygenase 2 augments osteoblastic but suppresses chondrocytic differentiation of CD90+ skeletal stem cells in fracture sites, *Sci. Adv.* 31 (2019), eaay2108.
- E.P. McNeill, S. Zeitouni, S. Pan, Characterization of a pluripotent stem cell-derived matrix with powerful osteoregenerative capabilities, *Nat. Commun.* 11 (2020) 3025.
- E. Cano, V. Gebala, H. Gerhardt, Pericytes or mesenchymal stem cells: is that the question? *Cell Stem Cell* 20 (2017) 296–297.
- W.L. Grayson, B.A. Bunnell, E. Martin, T. Frazier, B.P. Hung, J.M. Gimble, Stromal cells and stem cells in clinical bone regeneration, *Nat. Rev. Endocrinol.* 11 (2015) 140.
- W. Orapiriyakul, M.P. Tsimbouri, P. Childs, P. Campsie, J. Wells, Effects of electrospun submicron fibers in calcium phosphate cement scaffold on mechanical properties and osteogenic differentiation of umbilical cord stem cells, *Acta Biomater.* 7 (2011) 4037–4044.
- S. Yao, X. Lin, Y. Xu, Y. Chen, P. Qiu, C. Shao, B. Jin, Z. Mu, R. Tang, Osteoporotic bone recovery by a highly bone-inductive calcium phosphate polymer-induced liquid-precursor, *Adv. Sci.* 6 (2019), 1900683.
- S. Jin, D. He, D. Luo, Y. Wang, M. Yu, B. Guan, Y. Fu, Z. Li, T. Zhang, Y. Zhou, C. Wang, Y. Liu, A biomimetic hierarchical nanointerface orchestrates macrophage polarization and mesenchymal stem cell recruitment to promote endogenous bone regeneration, *ACS Nano* 13 (2019) 6581–6595.
- C. Goetsch, A. Babelova, O. Trummer, R.G. Erben, M. Rauner, S. Rammelt, N. Weissmann, V. Weinberger, S. Benkhoff, M. Kampschulte, B. Obermayer-Pietsch, L.C. Hofbauer, R.P. Brandes, K. Schröder, NADPH oxidase 4 limits bone mass by promoting osteoclastogenesis, *J. Clin. Invest.* 1123 (2013) 4731–4738.
- K.E. Ensrud, Bisphosphonates for postmenopausal osteoporosis, *JAMA* 325 (2021) 2017–2018.
- J. Sun, C.C. Mou, Q. Shi, B. Chen, X.L. Hou, W. Zhang, X.R. Li, J.W. Dai, Controlled release of collagen-binding SDF-1 $\alpha$  from the collagen scaffold promoted tendon regeneration in a rat Achilles tendon defect model, *Biomaterials* 162 (2018) 22–33.
- S.B. Coffelt, F.C. Marini, K. Watson, K.J. Zwezdaryk, J.L. Dembinski, H.L. LaMarca, S.L. Tomchuck, K.H. Bentrup, E.S. Danka, S.L. Henkle, A.B. Scandurro, The pro-inflammatory peptide LL-37 promotes ovarian tumor progression through recruitment of multipotent mesenchymal stromal cells, *Proc. Natl. Acad. Sci. Unit. States Am.* 106 (2009) 3806–3811.
- D. Park, J.A. Spencer, B.I. Koh, T. Kobayashi, J. Fujisaki, T.L. Clemens, C.P. Lin, H. M. Kronenberg, D.T. Scadden, Endogenous bone marrow MSCs are dynamic, fate-restricted participants in bone maintenance and regeneration, *Cell Stem Cell* 10 (2012) 259–272.
- A.D. Ellington, J.W. Szostak, In vitro selection of RNA molecules that bind specific ligands, *Nature* 346 (1990) 818.
- X. Xiong, H. Liu, Z. Zhao, M.B. Altman, D. Lopez-Colon, C.J. Yang, L.J. Chang, C. Liu, W. Tan, DNA aptamer-mediated cell targeting, *Angew. Chem. Int. Ed.* 52 (2013) 1472–1476.
- P. ecanale, D. Porciani, S. Pujals, A. Jurkevich, A. Chetrusca, Aptamers with tunable affinity enable single-molecule tracking and localization of membrane receptors on living cancer cells, *Angew. Chem. Int. Ed. Engl.* 59 (2020) 18546–18555.
- Z. Hou, S. Meyer, N.E. Propson, J. Nie, P. Jiang, R. Stewart, J.A. Thomson, Characterization and target identification of a DNA aptamer that labels pluripotent stem cells, *Cell Res.* 25 (2015) 390–393.
- C. Yao, H. Tang, W. Wu, J. Tang, W. Guo, D. Luo, D. Yang, Double rolling circle amplification generates physically cross-linked DNA network for stem cell fishing, *J. Am. Chem. Soc.* 142 (2020) 3422–3429.
- X. Hu, Y. Wang, Y. Tan, J. Wang, H. Liu, Y. Wang, S. Yang, M. Shi, S. Zhao, Y. Zhang, Q. Yuan, A difunctional regeneration scaffold for knee repair based on aptamer-directed cell recruitment, *Adv. Mater.* 29 (2017), 1605235.
- J. Son, J. Kim, K. Lee, J. Hwang, Y. Choi, Y. Seo, H. Jeon, H.C. Kang, H. Woo, B. Kang, J. Choi, DNA aptamer immobilized hydroxyapatite for enhancing angiogenesis and bone regeneration, *Acta Biomater.* 99 (2019) 469–478.
- S. Dong, Y. Chen, L. n Yu, K. Lin, X. Wang, Magnetic hyperthermia-synergistic H<sub>2</sub>O<sub>2</sub> self-sufficient catalytic suppression of osteosarcoma with enhanced bone-regeneration bioactivity by 3D-printing composite scaffolds, *Adv. Funct. Mater.* 30 (2020), 1907071.
- S. Li, Y. Xu, J. Yu, M.L. Becker, Enhanced osteogenic activity of poly(ester urea) scaffolds using facile post-3D printing peptide functionalization strategies, *Biomaterials* 141 (2017) 176–187.
- Y. Ma, J. Zheng, E.F. Amond, C.M. Stafford, M.L. Becker, Facile fabrication of "dual click" one- and two-dimensional orthogonal peptide concentration gradients, *Biomacromolecules* 14 (2013) 665–671.
- Ya Gabeta, R. Müller, E. Regev, J. Sela, A. Shteyer, K. Salisbury, M. Chorev, I. Bab, Osteogenic growth peptide modulates fracture callus structural and mechanical properties, *Bone* 35 (2004) 65–73.
- Y. Pei, M. Li, Y. Hou, Y. Hu, G. Chu, L. Dai, K. Li, Y. Xing, B. Tao, Y. Yu, C. Xue, Y. He, Z. Luo, K. Cai, An autonomous tumor-targeted nanoprodrg for reactive oxygen species-activatable dual-cytochrome c/doxorubicin antitumor therapy, *Nanoscale* 10 (2018) 11418–11429.
- J.C. Wu, C.S. Ruan, Y.F. Ma, Y.L. Wang, Y.F. Luo, Vital role of hydroxyapatite particle shape in regulating the porosity and mechanical properties of the sintered scaffolds, *J. Mater. Sci. Technol.* 34 (2018) 503–507.
- S.I. Jeong, E.K. Ko, J. Yum, C.H. Jung, Y.M. Lee, H. Shin, Nanofibrous poly(lactic acid)/hydroxyapatite composite scaffolds for guided tissue regeneration, *Macromol. Biosci.* 8 (2008) 328–338.
- R. Chakraborty, V.S. Seesala, S. Sengupta, S. Dhara, P. Saha, K. Das, S. Das, Comparison of Osteoconduction, cytocompatibility and corrosion protection performance of hydroxyapatite-calcium hydrogen phosphate composite coating synthesized in-situ through pulsed electro-deposition with varying amount of phase and crystallinity, *Surf. Interfaces* 10 (2018) 1–10.
- M. Sharma, R. Nagar, V.K. Meena, S. Singh, Electro-deposition of bactericidal and corrosion-resistant hydroxyapatite nanoslabs, *RSC Adv.* 9 (2019) 11170–11178.
- D.K. Khajuria, V.B. Kumar, D. Gigi, A. Gedanken, D. Karasik, Accelerated bone regeneration by nitrogen-doped carbon dots functionalized with hydroxyapatite nanoparticles, *ACS Appl. Mater. Interfaces* 10 (2018) 19373–19385.
- Y. Ha, J. Yang, F. Tao, Q. Wu, Y.J. Song, H.R. Wang, X. Zhang, P. Yang, Phase-transited lysozyme as a universal route to bioactive hydroxyapatite crystalline film, *Adv. Funct. Mater.* 28 (2018), 170446.
- R.A. Gittens, T. McLachlan, R. Olivares-Navarrete, Y. Cai, S. Berner, R. Tannenbaum, Z. Schwartz, K.H. Sandhage, B.D. Boyan, The effects of combined

- micron-/submicron-scale surface roughness and nanoscale features on cell proliferation and differentiation, *Biomaterials* 32 (2011) 3395–3403.
- [39] H. Yang, B. Jia, Z. Zhang, X. Qu, G. Li, W. Lin, D. Zhu, K. Dai, Y. Zheng, Alloying design of biodegradable zinc as promising bone implants for load-bearing applications, *Nat. Commun.* 11 (2020) 401.
- [40] Y. Hou, W. Xie, L. Yu, L.C. Camacho, C. Nie, M. Zhang, R. Haag, Q. Wei, Surface roughness gradients reveal topography-specific mechanosensitive responses in human mesenchymal stem cells, *Small* 16 (2020), e1905422.
- [41] F. Lüthen, R. Lange, P. Becker, J. Rychly, U. Beck, J.G. Nebe, The influence of surface roughness of titanium on beta 1- and beta3-integrin adhesion and the organization of fibronectin in human osteoblastic cells, *Biomaterials* 26 (2005) 2423–2440.
- [42] Y. Xu, W. Liu, G. Zhang, Z. Li, H. Hu, C. Wang, X. Zeng, S. Zhao, Y. Zhang, T. Ren, Friction stability and cellular behaviors on laser textured Ti-6Al-4V alloy implants with bioinspired micro-overlapping structures, *J. Mech. Behav. Biomed. Mater.* 109 (2020) 103823.
- [43] X. Tong, Q. Sun, D. Zhang, K. Wang, Y. Dai, J. Ma, C. Wen, J. Lin, Impact of scandium on mechanical properties, corrosion behavior, friction and wear performance, and cytotoxicity of a  $\beta$ -type Ti-24Nb-38Zr-2Mo alloy for orthopedic applications, *Acta Biomater.* 28 (2021) S1742–S7061.
- [44] K. Wang, X. Tong, J.X. Lin, M. Dargusch, C. Wen, Binary Zn–Ti alloys for orthopedic applications: corrosion and degradation behaviors, friction and wear performance, and Cytotoxicity, *J. Mater. Sci. Technol.* 74 (2021) 216–229.
- [45] P.H. Chen, Y.H. Tseng, Y. Mou, Y.L. Tsai, S.M. Guo, J.C. Chan, Adsorption of a statherin peptide fragment on the surface of nanocrystallites of hydroxyapatite, *J. Am. Chem. Soc.* 130 (2008) 2862–2868.
- [46] Q. Liu, S. Zheng, K. Ye, J. He, Y. Shen, S. Cui, J. Huang, Y. Gu, J. Ding, Cell migration regulated by RGD nanospacing and enhanced under moderate cell adhesion on biomaterials, *Biomaterials* 263 (2020) 120327.
- [47] C. Mu, Y. Hu, Y. Hou, M. Li, Y. He, X. Shen, K. Cai, Substance P-embedded multilayer on titanium substrates promotes local osseointegration via MSC recruitment, *J. Mater. Chem. B.* 8 (2020) 1212–1222.
- [48] S.D. Beco, K. Vaidziulytė, J. Manzi, Optogenetic dissection of Rac 1 and Cdc42 gradient shaping, *Nat. Commun.* 9 (2018) 4816.
- [49] P. Moreno-Layseca, J. Icha, H. Hamidi, J. Ivaska, Integrin trafficking in cells and tissues, *Nat. Cell Biol.* 21 (2019) 122–132.
- [50] J.Z. Kechagia, J. Ivaska, P. Roca-Cusachs, Integrins as biomechanical sensors of the microenvironment, *Nat. Rev. Mol. Cell Biol.* 20 (2019) 1–17.
- [51] C.T. Luk, S.Y. Shi, E.P. Cai, T. Sivasubramaniam, M. Krishnamurthy, J.J. Brunt, S. A. Schroer, D.A. Winer, M. Woo, FAK signalling controls insulin sensitivity through regulation of adipocyte survival, *Nat. Commun.* 8 (8) (2017), 14360.
- [52] P.M. Cromm, K.T.G. Samarasinghe, J. Hines, C.M. Crews, Addressing kinase-independent functions of fak via PROTAC-mediated degradation, *J. Am. Chem. Soc.* 140 (140) (2018) 17019–17026.
- [53] J. Block, H. Witt, A. Candelli, J.C. Danes, E.J.G. Peterman, G.J.L. Wuite, A. Janshoff, S. Köster, Viscoelastic properties of vimentin originate from nonequilibrium conformational changes, *Sci. Adv.* 13 (2018), eaay1161.
- [54] G.M. Policastro, F. Lin, L.A.S. Callahan, A. Esterle, M. Graham, K.S. Stakleff, M. L. Becker, p-OGP functionalized phenylalanine-based poly(ester urea) for enhancing osteoinductive potential of human mesenchymal stem cells, *Biomacromolecules* 16 (2015) 1358–1371.
- [55] A. Shellard, R. Mayor, All roads lead to directional cell migration, *Trends Cell Biol.* 30 (2020) 852–868.
- [56] X. Zhang, C. Zhang, Y. Lin, P. Hu, X. Deng, L. Chen, Nanocomposite membranes enhance bone regeneration through restoring physiological electric microenvironment, *ACS Nano* 10 (2016) 7279–7286.
- [57] A. Salhotra, H.N. Shah, B. Levi, M.T. Longaker, Mechanisms of bone development and repair, *Nat. Rev. Mol. Cell Biol.* 21 (2020) 696–711.
- [58] X. Fu, Y. Li, T. Huang, Z. Yu, K. Ma, M. Yang, J. Wang, M. Guan, Runx2/Osterix and zinc uptake synergize to orchestrate osteogenic differentiation and citrate containing bone apatite formation, *Adv. Sci.* 5 (2018), 1700755.
- [59] C.G. Zhang, W.L. Wang, X.D. Hao, Y. Peng, L.Q. Shao, G.Q. Li, A novel approach to enhance bone regeneration by controlling the polarity of GaN/AlGaIn heterostructures, *Adv. Funct. Mater.* 31 (2021), 2007487.
- [60] C. Wiraja, D.C. Yeo, M.S. Chong, C. Xu, Nanosensors for continuous and noninvasive monitoring of mesenchymal stem cell osteogenic differentiation, *Small* 12 (2016) 1342–1350.
- [61] M.N. Weitzmann, I. Ofotokun, Physiological and pathophysiological bone turnover - role of the immune system, *Nat. Rev. Endocrinol.* 12 (2016) 518–532.
- [62] C.S. Kovacs, C. Chaussain, P. Osdoby, M.L. Brandi, B. Clarke, R.V. Thakker, The role of biomineralization in disorders of skeletal development and tooth formation, *Nat. Rev. Endocrinol.* 17 (2021) 336–349.
- [63] K. Zhou, P. Yu, X. Shi, Hierarchically porous hydroxyapatite hybrid scaffold incorporated with reduced graphene oxide for rapid bone ingrowth and repair, *ACS Nano* 13 (2019) 9595–9606.
- [64] Y. Hu, S. Cao, J. Chen, Biomimetic fabrication of Icarin loaded nano hydroxyapatite reinforced bioactive porous scaffolds for bone regeneration, *Chem. Eng. J.* 394 (2020), 124895.
- [65] X. Li, Q. Zou, H. Chen, W. Li, In vivo changes of nanoapatite crystals during bone reconstruction and the differences with native bone apatite, *Sci. Adv.* 5 (2019), eaay6484.
- [66] P. Mora-Raimundo, D. Lozano, M. Benito, F. Mulero, M. Manzano, M. Vallet-Regi, Osteoporosis remission and new bone formation with mesoporous silica nanoparticles, *Adv. Sci.* 8 (2021), 2101107.
- [67] T. Wu, J. Sun, L. Tan, Q. Yan, L. Li, L. Chen, X. Liu, S. Bin, Enhanced osteogenesis and therapy of osteoporosis using simvastatin loaded hybrid system, *Bioact. Mater.* 5 (2020) 348–357.
- [68] N.R. Fuggle, E.M. Curtis, K.A. Ward, N.C. Harvey, E.M. Dennison, C. Cooper, Fracture prediction, imaging and screening in osteoporosis, *Nat. Rev. Endocrinol.* 15 (2019) 535–547.
- [69] B. Frediani, A. Giusti, G. Bianchi, L. Dalle Carbonare, N. Malavolta, L. Cantarini, G. Saviola, L. Molletta, Clodronate in the management of different musculoskeletal conditions, *Minerva Med.* 109 (2018) 300–325.
- [70] R.H. Zhang, X.B. Zhang, Y.B. Lu, W.H. Yuan, J. Wang, H.Y. Zhou, Calcitonin gene-related peptide and brain-derived serotonin are related to bone loss in ovariectomized rats, *Brain Res. Bull.* 176 (2021) 85–92.
- [71] O.G. Davies, P.R. Cooper, R.M. Shelton, A.J. Smith, B.A. Scheven, Isolation of adipose and bone marrow mesenchymal stem cells using CD29 and CD90 modifies their capacity for osteogenic and adipogenic differentiation, *J. Tissue Eng.* 6 (2015), 2041731415592356.
- [72] C. Mu, Y. Hu, Y. Hou, M. Li, Y. He, K. Cai, Substance P-embedded multilayer on titanium substrates promotes local osseointegration via MSC recruitment, *J. Mater. Chem. B.* 8 (2020) 1212–1222.